UNIVERSIDAD AUTÓNOMA DE NUEVO LEÓN

FACULTAD DE CIENCIAS QUÍMICAS

DYE-SENSITIZED SOLAR CELLS BASED ON BARE AND AU-DECORATED HEXAGONAL $ZnTiO_3$

Por

SUSANA BORBÓN ROJAS

Como requisito parcial para obtener el Grado de DOCTOR EN CIENCIAS con Orientación en Química de los Materiales

Agosto, 2022

DYE-SENSITIZED SOLAR CELLS BASED ON BARE AND AU-DECORATED HEXAGONAL $ZnTiO_3$

Aprobación de la Tesis:

Dr. Israel A. López Hernández

Presidente

Dr. Eduardo Maximino Sánchez Cervantes

Secretario

Dra. Yolanda Peña Méndez

Vocal I

Dra. Adela Verónica González Pérez

Vocal II

Dra. Nayely Pineda Aguilar

Vocal III

Dra. María Elena Cantú Cárdenas

Sub-Directora de posgrado

DYE-SENSITIZED SOLAR CELLS BASED ON BARE AND AU-DECORATED HEXAGONAL $ZnTiO_3$

Revisión:

Dr. Israel A. López Hernández

Director

Dra. Shadai Lugo Loredo

Co-directora

Dra. Yolanda Peña Méndez

Tutor 1

Dr. Eduardo Maximino Sánchez Cervantes

Tutor 2

Dr. Alejandro Vázquez Dimas

Tutor 3

Dra. María Elena Cantú Cárdenas

Subdirectora de posgrado

RESUMEN

Susana Borbón Rojas Fecha de graduación: Agosto, 2022

Universidad Autónoma de Nuevo León

Facultad de Ciencias Químicas

Título de la tesis: DYE-SENSITIZED SOLAR CELLS BASED ON BARE AND AU-DECORATED HEXAGONAL $ZnTiO_3$

Número de páginas: 98 Candidato para el título de Doctor en Ciencias con Orientación en Química de los Materiales

Área de estudio: Materiales Funcionales

Propósito y método del estudio: Para fabricar celdas solares sensibilizadas con colorante (DSSC) la síntesis de nuevos óxidos semiconductores para su aplicación como material de fotoánodo es de interés. En este trabajo se reporta el aumento en el voltaje de circuito abierto (V_{OC}) de una DSSC con un fotoánodo de nanoestructuras de $ZnTiO_3$, sintetizado por método sol-gel, decorado con nanopartículas de Au. Los dispositivos solares fueron caracterizados por sus curvas corriente-potencial (J-V) y espectroscopía de impedancia electroquímica (EIS).

Contribuciones y conclusiones: Se desarrolló una síntesis sol-gel en condiciones atmosféricas sin el uso de aditivos, surfactantes para la obtención de nanopartículas de $ZnTiO_3$ en fase hexagonal. Las más eficientes DSSC alcanzaron una eficiencia de conversión de energía de 0.18%.

Firma del Asesor:_____

ABSTRACT

Susana Borbón Rojas Graduation date: August, 2022

Universidad Autónoma de Nuevo León

Facultad de Ciencias Químicas

Title of the study: DYE-SENSITIZED SOLAR CELLS BASED ON BARE AND AU-DECORATED HEXAGONAL $ZnTiO_3$

Number of pages: 98 Candidate to the degree of Doctor of Science in Materials Chemistry

Area of study: Functional Materials

Purpose and method of the study: The synthesis of new semiconducting oxides for its application as photoanode material in dye-sensitized solar cells (DSSC) is an on-going research topic. In this work we report the improvement in the open-circuit voltage (V_{OC}) of a DSSC with a photoanode of $ZnTiO_3$ nanostructures, synthetized by sol-gel method and decorated with Au nanoparticles. The solar cells were characterized by its current-voltage curves (J-V) and electrochemical impedance spectroscopy (EIS).

Contributions and conclusions: A sol-gel method for the synthesis of $ZnTiO_3$ nanoparticles in hexagonal phase in atmospheric conditions and without additives or surfactants was developed. The best DSSC had an energy conversion efficiency of 0.18%.

Advisor's signature:_____

ACKNOWLEDGEMENTS

Gracias al CONACYT por la beca otorgada (762227). Agradezco a mi asesor el Dr. Israel López por compartir sus conocimientos durante estos años de formación, por integrarme en su grupo de investigación, y por todo su apoyo para la realización de este proyecto. Así también agradezco a mi co-asesora la Dra. Shadai Lugo por su guía y soporte.

Agradecimientos a mi comité tutorial, la Dra. Yolanda Peña, el Dr. Alejandro Vázquez y el Dr. Eduardo Sánchez por sus acertados comentarios y consejos. Especialmente al Dr. Eduardo y la Dra. Yolanda por brindarme acceso a sus laboratorios y sus equipos de caracterización. Agradezco también a la Dra. Nayely Pineda del CIMAV-Monterrey por su valioso apoyo con las caracterizaciones de FE-SEM y EDXS. Gracias al Dr. Isaac Zarazúa de la Universidad de Guadalajara por compartir sus conocimientos acerca de dispositivos fotovoltaicos, lo cual marcó una gran diferencia en la realización de este trabajo de tesis.

Agradezco especialmente al Dr. Manuel Quevedo de The University of Texas at Dallas por abrirme las puertas de su laboratorio y su grupo de trabajo. Su apoyo brindó una experiencia única que me ha permitido adquirir conocimiento practico de múltiples técnicas de caracterización, y que sin lugar a duda complementó ampliamente mi formación como doctor en ciencias.

Agradezco a mis papás por su apoyo incondicional durante toda mi formación. Sin su apoyo y su ejemplo no sería la persona que soy el día de hoy. Gracias a

mi hermano por mostrarme el más grande modelo de fortaleza y por inspirarme a seguirme esforzando día y día.

Finalmente quiero agradecer a mi esposo y colega Eder Cedeño. Gracias por ser el motor de mi vida y navegar a mi lado durante estos tres años llenos de retos, cambios y sobre todo mucho aprendizaje. Gracias por tu apoyo incondicional (académico y personal), por tus insights y por las interesantes discusiones acerca de nuestras tesis.

CONTENT TABLE

LIST OF FIGURES

LIST OF TABLES

NOMENCLATURE

A	Active area
A.M.	Air Mass
a.u.	Arbitrary units
AC	Alternating current
$C\mu$	Chemical capacitance
DC	Direct current
Dn	Chemical diffusion coefficient
DRS	Diffuse reflectance spectroscopy
DSSC	Dye sensitized solar cell
E_c	Conduction band
EDS	Energy dispersive spectroscopy
E_g	Bang gap energy (eV)
EIS	Electrochemical impedance spectroscopy
E_v	Valence band
FE-SEM	Field-emission scanning electron microscopy
FF	Fill factor
FTO	Fluorine-doped tin oxide
ICP-OES	Inductively coupled plasma optical emission spectroscopy
ITO	Indium tin oxide
J-V	Current-voltage
J	Current density (mA cm^{-2})

Jmax	Maximum current density (mA cm^{-2})
JSC	Short circuit current density (mA cm^{-2})
K	Dimensionless shape factor
LSPR	Localized surface plasmon resonance
LUMO	Lowest unoccupied molecular orbital
PCE	Power conversion efficiency
$Pmax$	Maximum power (W)
$Psun$	Light intensity per unit area (mW cm^{-2})
QDSSC	Quantum dot sensitized solar cell
R	Reflectance
RCT	Recombination resistance (Ω)
Rd	Diffusion impedance in the electrolyte
Rpm	Revolutions per minute
RPt	Transfer resistance in the counter electrode (Ω)
Rrec	Recombination resistance at the interface of the semiconductor, the electrolyte and the chemical capacitance (Ω)
Rs	Series resistance (Ω)
SPR	Surface plasmon resonance
$T_{1/2}$	Electron lifetime (s)
UV-Vis	Ultraviolet-visible
V	Voltage (V)
V_{OC}	Open circuit voltage (mV)
XRD	X-ray diffraction

β	Light broadening at half the maximum intensity
θ	Bragg angle
λ	Wavelength (nm)
τ	Crystallite size

CHAPTER 1

INTRODUCTION

Since the rise of industry in the second half of the XVIII century, there has been a continuous increase in the energy demand that does not appear to diminish. The energy consumption trend has been going upwards as the population and the industry continues to increase [1]. Ever since the industrial revolution took place, mankind has relied on the burning of fossil fuels to produce energy, but this dependence has left its mark on the planet. Due to the intense and continuous use of fossil fuels during the past century, there has been an alarming increase in green-house gases emissions [2]. These gases alter the climate of the planet by trapping heat in the atmosphere, effect that is known as green-house effect. Among the green-house gases are water vapor, carbon dioxide, methane, ozone, nitrous oxides and fluorocarbons [3].

To stop the emissions of green-house gases, our society must switch to the use of renewable energy, which does not produce emissions. Some examples of these are geothermal, hydroelectric, wind and solar energy, being the last mentioned the most abundant in terms of availability of resources [4,5].

Among the benefits of the use of solar energy, in addition to its abundance, is the fact that it is renewable, inexhaustible in human time scale, non-polluting, reduces energy imports and it can be applied for large-scale electricity generation or in small-scale in isolated areas [4]. Since Mexico exhibits a favorable geographical location, it can receive up to 6.15 kW h/m^2 of solar irradiation [6].

1.1 Photovoltaic cells

Solar cells have been developed to change solar energy to electric energy. So far the photovoltaic devices can be classified in three [7]. While the technology of the first and second generation are mature, the third one is still in a development phase.

Third generation of solar cells are assembled of inorganic nanoparticles and organic macromolecules, and hybrids of these two. Amid its many advantages, this generation of solar cells are non-toxic and inexpensive to fabricate [8,9]. As a subclassification for inorganic solar cells, dye-sensitized solar cells (DSSC), quantum-dot sensitized solar cells (QDSSC) and perovskite solar cells are found. In this work we will synthesize and characterize a novel photoanode material and for its application in DSSC.

1.2 Dye-sensitized solar cells (DSSC)

DSSC are among the most promising alternatives of solar technology, because of its low-cost components and easy assembly process [10]. In addition, they possess several advantages over existing solar technology [11,12]:

- They are efficient under diffuse light
- They do not have to be fabricated from single-crystalline materials
- They can be fabricated onto flexible substrates
- They are multi-colored and transparent
- They are non-toxic

However, they are not perfect and present some disadvantages. Some of the possible drawbacks are related to the use of a liquid electrolyte, such as its evaporation if the device is not appropriately sealed and its instability at low and high temperatures.

Although being a solar cell, DSSC are based on the natural phenomenon of photosynthesis, hence they are a photoelectrochemical system [13]. DSSC are built by:

- Photoanode: Semiconductor nanoparticles over a conducting glass substrate and sensitized with dye molecules.
- Counter electrode: which is constituted by a conducting glass substrate with a deposited catalyst.
- Electrolyte between counter electrode and photoanode.

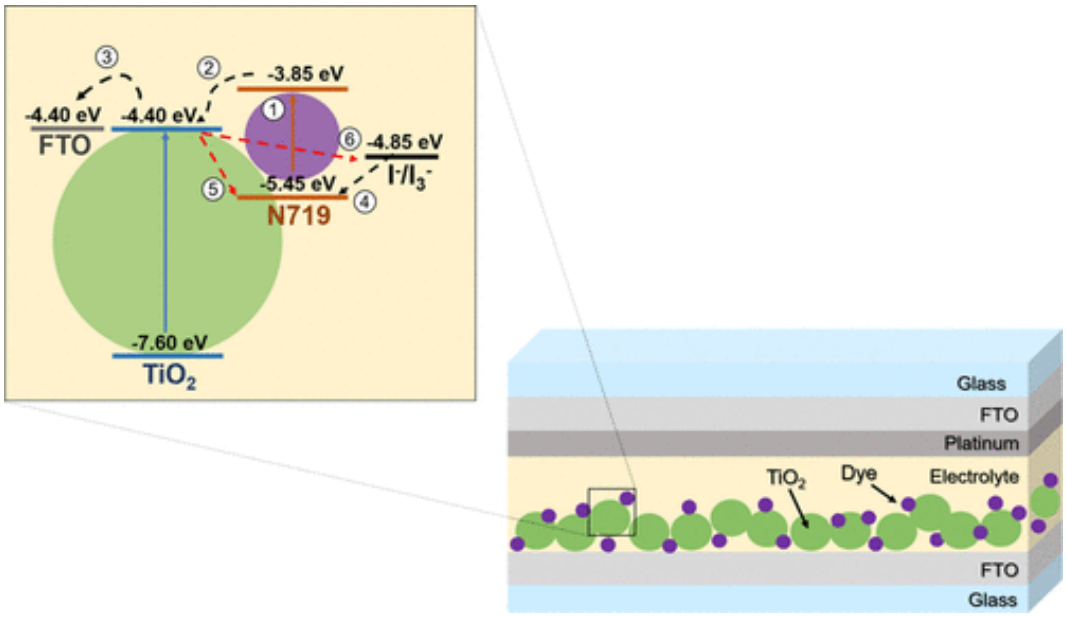

Figure 1. DSSC scheme illustrating the architecture and work principle. (1) excited state generation, (2) electron injection, (3) electron transport, (4) dye's regeneration, (5,6) recombination in dye and electrolyte, respectively [14].

1.3 DSSC mechanism

As aforementioned, DSSC imitates the natural process of photosynthesis. Whilst photosynthesis produces glucose molecules, DSSC can offer electricity from solar spectrum without a chemical degradation [15].

As sunlight falls upon the DSSC, photons are absorbed onto semiconductor nanoparticles by chemisorbed dye molecules. Thus, an oxidizing process starts (Eq. 1) where an electron is excited from the dye molecule from the HOMO level to the LUMO level. Then, the free electron is injected to the conduction band (Eq. 2) as long as the LUMO level of the dye is higher than the conduction band edge of the semiconductor. Moreover, other factors as the energy difference between the dye energy level and the semiconductor conduction band will impact in the electron

injection rate [15]. As the electrons travel to the conduction band of the semiconductor, they reach the conductive substrate. So, electrons can reduce the redox mediator (Eq. 3) which regenerates the dye (Eq. 4) closing the circuit. To ensure the regeneration of the dye, the dye HOMO level must lie lower than the energy level of the electrolyte [16]. However, a recombination process can occur where the electron can regenerate the electrolyte or the oxidized dye (Eq. 5, and Eq. 6).

$$S_{(adsorbed)} + hv \rightarrow S^{*}_{(adsorbed)} \quad \text{Eq. 1}$$

$$S^{*}_{(adsorbed)} \rightarrow S^{+}_{(adsorbed)} + e^{-}_{(injected)} \quad \text{Eq. 2}$$

$$I_3^- + 2e^-_{(counter\ electrode)} \rightarrow 3I^-_{(counter\ electrode)} \quad \text{Eq. 3}$$

$$S^{+}_{(adsorbed)} + \frac{3}{2} I^- \rightarrow S_{(adsorbed)} + \frac{1}{2} I_3^- \quad \text{Eq. 4}$$

$$S^{+}_{(adsorbed)} + e^-_{(semiconductor)} \rightarrow S_{(adsorbed)} \quad \text{Eq. 5}$$

$$I_3^- + 2e^-_{(semiconductor)} \rightarrow 3I^- \quad \text{Eq. 6}$$

1.4 Materials and components

Substrate

In DSSC, the substrate plays four principal functions; 1) as a physical support where the semiconductor coating sticks, 2) endows electric contact, 3) collects the produced electrons and 4) entitles sunlight absorption.

The substrate consists of conductive oxide thin film which should be transparent to the visible light and exhibit low electrical resistivity [17]. The most popular conductive

oxide (TCO) in DSSC is fluorine-doped tin oxide (FTO); however, indium-doped zinc oxide (IZO) and indium or antimony-doped tin oxide (ITO, ATO) and are also employed.

Sensitizers

Sensitizers or dyes absorbs photons and produce electrons which are transferred to the semiconductor. Its structure is chemisorbed to the semiconductor providing DSSC with its characteristic colors.

Dyes must satisfy some requirements [16,18]:

- A high molar absorption coefficient, hence the dye is chemisorbed to the semiconductor's surface. The best performing dye, cisbis(isothiocyanato)bis(2,2′-bipyridyl-4,4′-dicarboxylato)-ruthenium(II) bistetrabutylammonium (N719), possess a molar absorption coefficient of 1.26 $x10^4$ M^{-1} cm^{-1} [19].
- Possess hydroxyl and carboxyl groups which allow them binding to the surface.
- Absorb a widen region of the visible spectrum.
- The HOMO and LUMO energies must fit with the electrolyte and the semiconductor energy levels.
- A high regeneration rate.
- Photostability in a wide range of temperatures.
- Soluble in organic solvents.

A classification of dyes in DSSC can be done as: metal complex dyes, metal-free organic dyes and natural dyes.

Electrolyte

The electrolyte endows ion conductivity because of its diffusion through the semiconductor. To achieve a high efficiency the electrolyte must be [8]:

- Transparent
- Non-reactive with other solar cell components
- Highly soluble
- Thermodynamically stable

Iodide-triiodide, I_3^-/I^-, is the most popular electrolyte [16] with the efficiencies so far.

Counter electrode

The counter electrode is formed by a conductive substrate with a catalyst which must comply several requirements [20]:

- Be inert with the other components
- High electrocatalytic activity
- Be chemically stable against the electrolyte
- Have high conductivity
- Have high electron mobility

Platinum has been the most popular catalyst in DSSC because it complies with all the aforementioned requirements [21].

Photoanode materials

On the other hand, the photoanode plays a different role in DSSC. It collects and transports the electrons to the back contact, and the efficiency of the solar cells relies on its properties. Photoanodes of devices with higher efficiencies must exhibit [22]:

- A wide band-gap energy
- High surface area
- High electron mobility
- Mesoporosity
- Resistance to photo-corrosion
- Roughness in the surface for chemisorption processes
- Light-scattering ability
- Be earth-abundant and environmentally friendly

So far, due to its wide band gap energy (3.2 eV) and high conduction band the most used semiconductor is TiO_2. Even though TiO_2 devices have achieved the highest efficiencies [23], its electron mobility is low (0.1-4 cm^2/Vs) [24]. Wurtzite ZnO is considered the second most employed semiconductor in DSSC with a band gap energy of 3.37 eV and electron mobility in the range of 200-300 cm^2/Vs [5,25,26]. Though having higher electron mobility, the ZnO DSSC devices have not overcome the efficiency of TiO_2 devices [27,28]. Its low efficiency has been ascribed to a low electron injection in the material, promoting electron recombination [28], and to its

chemical instability in acidic solutions [29–31]. Therefore, the development for a better DSSC photoanode material is cutting-edge research where new materials are being tested, such as Nb_2O_5 [32], SnO_2 [33], $SrTiO_3$, In_2O_3, WO_3 [34] and zinc titanates [35].

1.5 Zinc titanates

Zinc titanates are form by a TiO_2-ZnO binary system which depending on synthesis method stoichiometry and thermal treatment temperature can give rise to three different crystalline structures; $ZnTiO_3$ (cubic, hexagonal), Zn_2TiO_4 (cubic, tetragonal) and $Zn_2Ti_3O_8$ (cubic) [36,37]. In accordance to the literature, at temperatures under 600 °C, between 600 and 945 °C and above 945 °C, $Zn_2Ti_3O_8$, $ZnTiO_3$, Zn_2TiO_4, can be obtained considering a ratio stoichiometry 1:1. However, depending on the synthesis method and the reactants used a different level of purity is obtained.

Hexagonal $ZnTiO_3$ is one of the most promising semiconductors in applications such as photocatalysis, solar cells, gas sensors, and paint and antibacterial applications [36,38]. Hexagonal $ZnTiO_3$ has a perovskite structure ABO_3 [39], with BO_6 octahedra with A^+ cations inserted in the crystalline structure. Because of its wide band-gap energy (2.96 eV) and superior electron mobility (150-400 cm^2/vs), is also a favorable alternative for DSSC's photoanode material [40]. Moreover, the energy of its conduction and valence band makes it suitable to be used in DSSC with the most used and best performing dye and electrolyte, N719 dye and I_3^-/I^- respectively. In

Figure 2 is shown a schematic diagram of the energy levels of a DSSC with $ZnTiO_3$ as semiconductor, N719 as dye and I_3^-/I^- as electrolyte, where it can be seen that the conduction band position of the $ZnTiO_3$ assures the electron injection from the dye.

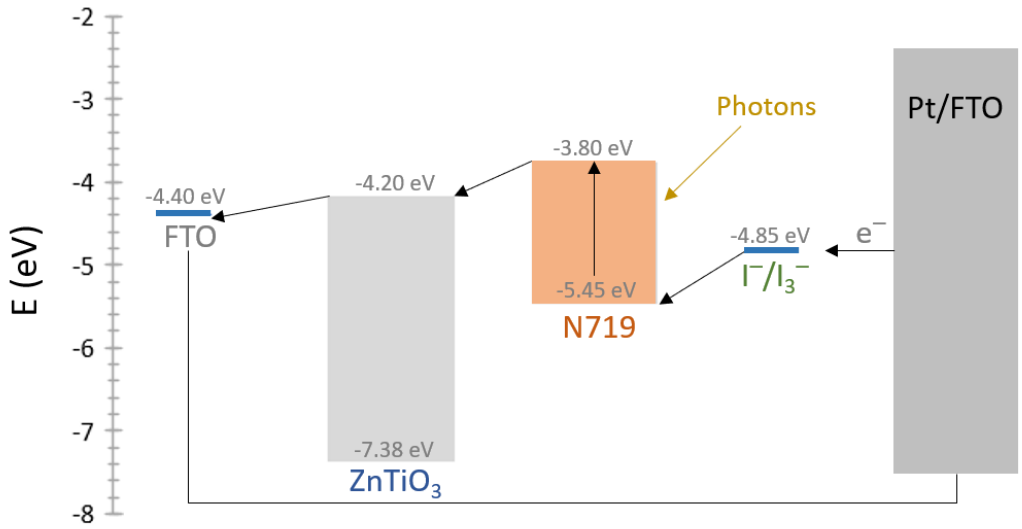

Figure 2. Schematic diagram of energy levels of a DSSC with $ZnTiO_3$ as semiconductor, N719 dye and I_3^-/I^- as electrolyte.

$ZnTiO_3$ has been synthesized by a plethora of methods such as; solid-state reaction [41], sol-gel method [42], molten salt [43], carbothermal method [44], evaporation-induced self-assembly method [45] and hydrothermal method. Among them, sol-gel method stands out due to its advantages over the others, such as high product purity, reduction of sintering temperature, low cost and easy reactant adjustment [46,47]. Furthermore, it has been proved that by changing the temperature of the thermal treatment of the gel, it is possible to obtain cubic or hexagonal crystalline structure [39].

1.6 Sol-gel synthesis

Sol-gel is a technique that allows the synthesis of high purity nanomaterials with a homogeneous distribution of the components [48] . Among its advantages over other methods is the fact that it is performed under low temperatures, it provides a high yield, it has low production cost and great control over the physicochemical properties of the products. Furthermore, by controlling several parameters it is possible to tune the properties of the products, such as; concentration and type of precursors, solvent used, pH of the reaction medium, type and concentration of additives, aging time and pre- and post-heat treatment of the products. A schematic representation of the sol-gel process is depicted in Figure 3.

Sol-gel synthesis is performed in the following steps:

- Preparation of the precursors' solutions.
- Sol formation by hydrolysis and partial condensation of alkoxides.
- Gel formation by polycondensation of hydrolyzed precursors.
- Drying of the gel by evaporation of the solvent.
- Thermal treatment for the obtention of mechanically stable materials.

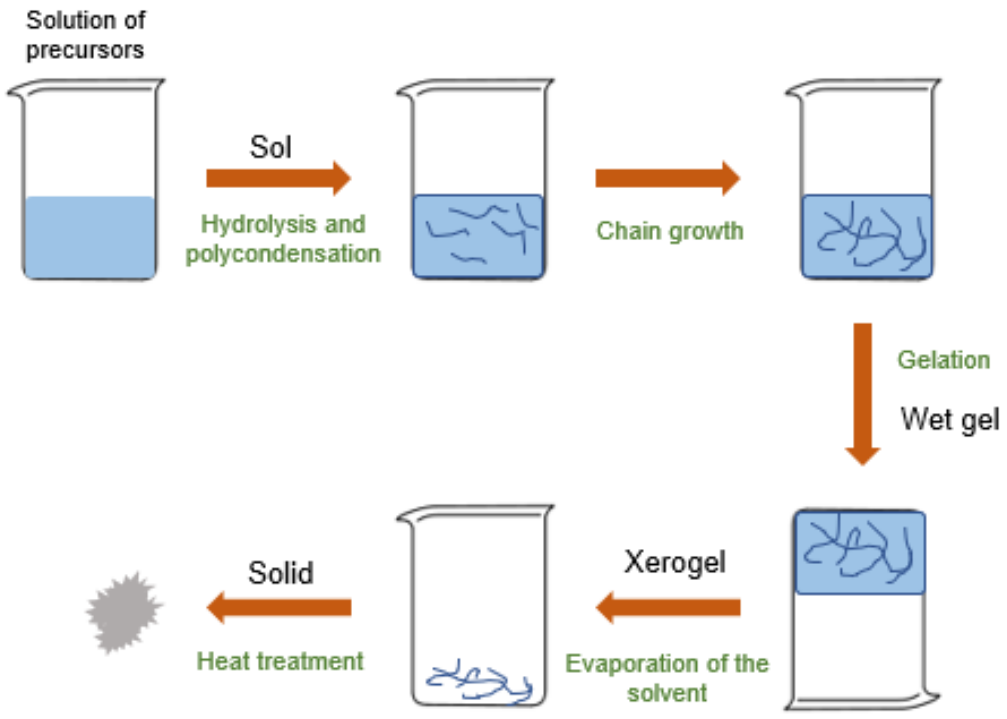

Figure 3. Schematic representation of sol-gel synthesis.

An aging step may be added because the chemical reactions continue after the formation of the gel, causing changes in the structure, composition, and properties. These reactions do not stop until all the solvent is evacuated from the gel, which happens during the drying step.

The principal reactions in sol-gel synthesis are hydrolysis and polycondensation, and the result of both is the gelation [47].

In the hydrolysis a nucleophilic substitution is done, resulting in the replacement of an alkoxy group with a hydroxyl.

$$\equiv M - OR + HOH \leftrightarrow \equiv M - OH + ROH \qquad \text{Eq. 7}$$

At the same time hydrolysis occur also the polycondensation happens. In polycondensation the partially hydrolyzed alkoxide react with another hydroxyl group removing water or produce an alcohol molecule reacting with an alkoxy group.

$$\equiv MOH + \equiv MOH \leftrightarrow \equiv M - O - M + HOH \qquad \text{Eq. 8}$$

$$\equiv MOH + \equiv MOR \leftrightarrow \equiv M - O - M + ROH \qquad \text{Eq. 9}$$

Both reactions, hydrolysis and polycondensation lead to the formation of a 3-D polymeric structure, the gel. The gel forms due to the formation of clusters that bind each other, which produces an abrupt increase in the viscosity.

In the drying the wet gel is heated at temperatures above 100 °C to desorb water and alcohol that are bounded to the structure. Different methods of drying give different structures, such as xerogels, aerogels, thin films, among others. The simplest drying method, simple evaporation leads to the formation of a xerogel, which is characterized by a disordered porosity and the formation of cracks.

In the sol-gel synthesis of $ZnTiO_3$ a thermal treatment is needed for the obtention of the crystalline structure, treatments up to 900 °C are performed.

1.7 Semiconductors

Without semiconductors the rise of electronic and optoelectronic devices would have not been possible. Semiconductor materials are any class of crystalline solids whose electrical properties are between those of conductors and insulators. Depending on its nature, two types of semiconductors exist [49]:

- Intrinsic: Its conductivity is inherent of the material, such as silicon or germanium.
- Extrinsic: Its conductivity relies on the impurities. They can be subclassified in type n and p.
    - Type n are semiconductors doped by five valence electrons impurities like arsenic, antimony, phosphorus, also called donors.
    - Type p are semiconductors doped by three valence electrons elements, like aluminum, boron, gallium, also called acceptors.

Two types of charge carriers are present in semiconductors: holes, with positive charge and conduction electrons, with negative charge. These mobile particles, known as charge carriers, are responsible for transporting charge, hence the production of electrical current [50].

According to band theory, bands of energy form because of the combination of molecular orbitals close in energy and the difference between them is known as band-gap (Eg). The energy bands in semiconductors correspond to the unfilled band and the filled band, known as valence band and conduction band respectively. In Figure 4 is shown a schematic representation of the bands and the Eg.

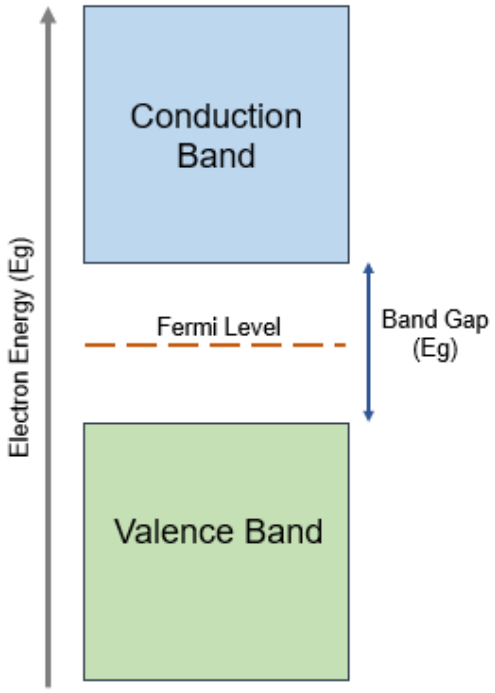

Figure 4. Energy band diagram of intrinsic semiconductors.

Another important parameter in semiconductors is the Fermi level. The first description of the Fermi level is the electrochemical potential of electrons. The second description defines the Fermi level as the top of the collection of electron energy levels at absolute zero [51].

In intrinsic semiconductors the number of holes is equal to the number of electrons in the conduction band, hence its probability of occupation of energy levels is the equivalent. Consequently, the Fermi level lies in the middle of the band gap. The Fermi level is important in DSSC because its difference with the energy of the redox material gives the open circuit voltage [52].

Additionally, other important semiconductor parameter in DSSC is the conductivity. The conductivity is defined as the product of the number of carriers (electrons or holes), their charge and its mobility

$$\sigma = (ne\mu_e + pe\mu_h) \qquad \text{Eq. 10}$$

where n and p are the concentrations of electrons and holes, respectively, e is the electron charge and μ_e and μ_h the electron and hole mobilities. Being the mobility the ratio of the drift velocity of a charge carrier per unit electric field.

$$\mu = \frac{|v|}{E} \qquad \text{Eq. 11}$$

1.8 Nanotechnology

Nanotechnology is defined as the technology that includes materials in the nanoscale. For a material be considered a nanomaterial it must have at least one of its dimensions below 100 nm [53]. When in the nanoscale the chemical, mechanical, thermal, optical, electrical, and magnetic properties of a material are modified due to quantum confinement effects [54]. Quantum confinement effect occurs when the nanoparticle size approximates a critical quantum measurement, the exciton Bohr radius. Quantum confinement leads to the separation of the continuous energy bands into discrete energy levels separated by potential barriers, so the motion of carriers is constricted or confined. Because the electrons are confined in a small space, they sense the presence of the particle frontiers and respond to it by adjusting its energy [55].

1.9 Plasmonics

A plasmon is a quasiparticle formed by the collective vibration of electrons in a metal. This happens when electromagnetic radiation and the metal interact. The principal requirement for the existence of the plasmon is that the dipole surface plasmon resonance frequency and irradiating light energy must be the same [56].

Plasmonic nanoparticles display a spectral response ascribed to the surface plasmon resonance (SPR) phenomenon. SPR occurs when specific radiation wavelengths hit the metal, triggering the collective oscillation of the electrons, they are also originated from the difference in dielectric constant between the metallic nanoparticle and the non-conductive environment. Nonetheless, these electrons are not able to propagate through the material which induces the localized surface plasmon resonance (LSPR) (Figure 5). The LSPR provokes large increment of the localized electromagnetic field in the vicinity of the plasmonic nanoparticle. LSPR is a characteristic property of noble metal nanoparticles, particularly in gold, silver, copper and aluminum [53].

Recent research works have used the LSPR of noble metal nanoparticles to improve the energy conversion efficiency of DSSC by taking advantage of various phenomena; enhance of the light-harvesting of the dye molecules due to the increase of the near fields, shift of the Fermi level of the semiconductor, light scattering induced by the plasmonic nanoparticles and augmenting the electron density (photocharging effect) [57].

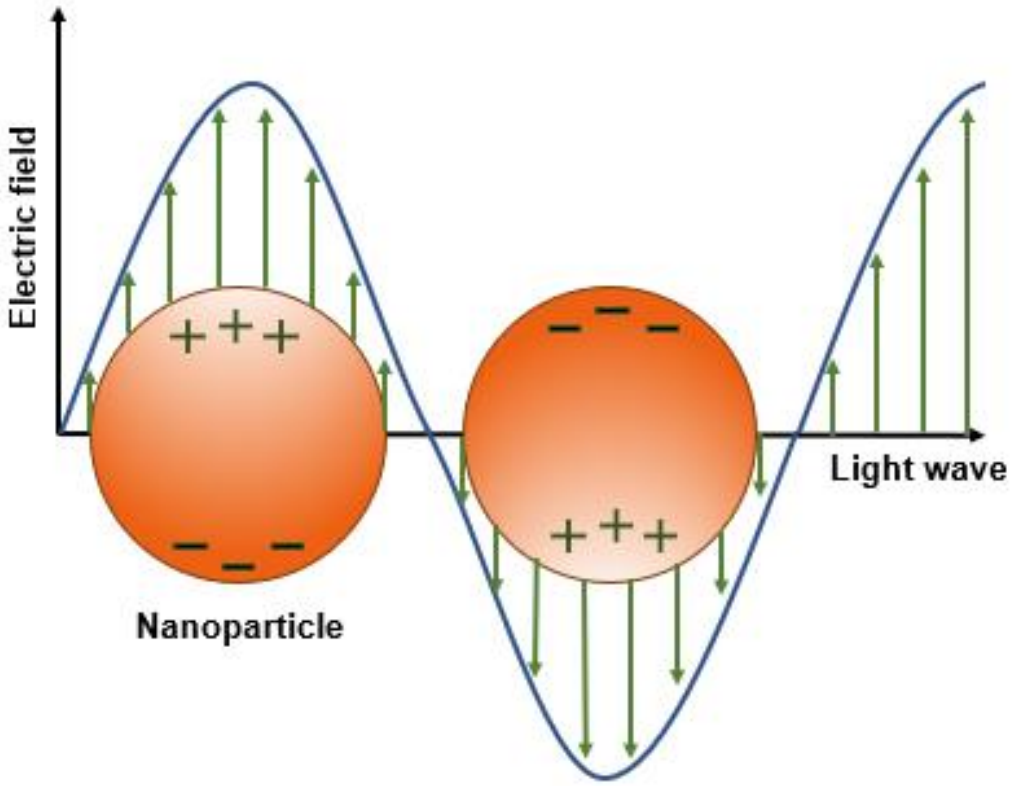

Figure 5. Schematic representation of a plasmon.

CHAPTER 2

BACKGROUND

The first DSSC was developed in 1991 by M. Gratzel and O'Regan [58], even though the concept of imitating the natural phenomenon of photosynthesis has been around since 1974 [59]. The novelty of the photovoltaic device assembled in 1991 is that it is a photoelectrochemical system hence, it has a completely different functioning mechanism than the solar cells based on a p-n junction. The photovoltaic cell of Gratzel and O'Regan, with a photoanode of anatase TiO_2 nanoparticles, yielded an energy conversion efficiency of 7.1-7.9%.

Ever since, the principal structure of DSSC has remained, while the materials of the components materials have been varied, achieving efficiencies of up to 14% [60]. But one of the most studied parts of the DSSC are the photoanode materials; to date the most used semiconductor in DSSC has been anatase TiO_2, while the second most used is wurtzite ZnO [61].

Recently, to incorporate the best properties of both semiconductors, composite TiO_2-ZnO materials have been applied in photovoltaic processes and photocatalytic reactions [62–65].

Habibi *et al.* [66] fabricated and compared DSSC based on hexagonal $ZnTiO_3$, wurtzite ZnO and anatase TiO_2 in 2012. They synthesized the semiconductor nanoparticles by sol-gel technique and deposited the material on FTO substrates by doctor blade. They used the dye E)-3-(5-(4-(bis(2',4'-dibutoxy-[1,1'-biphenyl]-4-yl)amino)phenyl)thiophen-2-yl)-2-cyanoacrylic acid (D35) and $Co(bpy)_3^{2/3+}$ as electrolyte for the three cells. The semiconductor particles were characterized by XRD, SEM, and DRS, and the J-V curves of the cells were obtained. Their results exhibited a diminution trend of V_{OC} and J_{SC} of ZnO>$ZnTiO_3$>TiO_2. Their work was focused on the photovoltaic performance of the DSSC rather that the synthesis and material's characterization, especially $ZnTiO_3$. Therefore, a deeper report on $ZnTiO_3$ characterization and application on DSSC, including electrochemical characterizations, is required to further confirm its performance in these devices.

In 2014, Sarkar *et al*. [35] worked with a compound of ZnO/TiO_2; they synthesized foam-like zinc orthotitanate (Zn_2TiO_4), in cubic phase, via template-assisted sol-gel route, and deposited it on fluorine-doped tin oxide (FTO) substrates by spray-deposition. First, TiO_2 and ZnO sols were prepared, followed by its mixing, deposition, and thermal treatment at 600 °C. They varied the thickness of the deposit from 4 to 10 μm, and the DSSC were assembled using the dye 5-[[4-[4-(2,2-Diphenylethenyl)phenyl]-1,2,3-3a,4,8b-hexahydrocyclopent[b]-indol-7-yl]methylene]-2-(3-ethyl-4-oxo-2-thioxo-5-thiazolidinylidene)-4-oxo-3-thiazo-

lidineacetic acid (D149) and I_3^-/I^- as electrolyte. The device with a thickness of 10 μm achieved the best performance with a J_{SC} of 4.6 mA cm^{-2}, V_{OC} of 724 mV, FF of 0.43 and efficiency (η) of 1.5%. Even though their research focused on the synthesis and characterization of the Zn_2TiO_4 rather than device optimization, it shows the potential application of zinc titanates in DSSC.

In 2016, Yu *et al.* [40] assembled a quantum-dot sensitized solar cell (QDSSC) with $ZnTiO_3$ as photoanode and investigated them theoretically and experimentally. Their calculations, made by density functional theory (DFT), exhibited promising results for the application of the material in QDSSC, due to its band-gap energy of 2.96 eV and high electron mobility of 150-400 cm^2/Vs. To probe its calculations, they synthesized hexagonal $ZnTiO_3$ nanoparticles by sol-gel method. The final $ZnTiO_3$ exhibited pure hexagonal crystalline phase and average particle size of 250-300 nm. The QDSSC was assembled with the architecture $ZnTiO_3$/CdS/CdSe, obtaining a J_{SC} of 5.96 mA cm^{-2}, 590 mV as V_{OC}, FF of 0.56 and efficiency of 1.95%. Although QDSSC and DSSC are very similar its difference relies on the sensitizer; on QDSSC the organometallic or organic dyes are replaced by nanoparticles of CdS, CdSe, PbS, PbSe or InP. Even though quantum dots can be modified to tune its band-gap energy over a broad spectral range, they are toxic and have insufficient light absorption and promote the electron recombination in the interface of quantum dot-semiconductor-electrolyte, thus limiting the device efficiency [67].

In 2018, Noor *et al.* [68] synthesized anatase TiO_2 and wurtzite ZnO particles (with a diameter of 30 nm) by sol-gel technique and blend both materials in different weight percentages (10%, 15%, 30% and 50%) by chemical impregnation. The final

composited were used as photoanodes in DSSC, with N719 as dye and I_3^-/I^- as electrolyte. The assembled devices showed a higher efficiency with the incorporation of ZnO, due to Ti-O-Zn linkage, to which was attributed the diminution of the band-gap energy of the composite and the reduction of electron recombination. Ti-O-Zn linkage was confirmed by Fourier-transformed infrared spectroscopy (FT-IR) and electrochemical impedance spectroscopy (EIS) gave the electron recombination rate. The DSSC with 15% of ZnO exhibited an efficiency of 2.8%, the best among all the devices, with a V_{OC} of 450 mV, J_{SC} of 8.4 mA cm^{-2}, and FF of 0.75. Its higher efficiency was related to its superior dye loading among all the other DSSC.

It is known that high surface area and adsorption energy are needed to improved electron injection from the excited dye molecule to the semiconductor conduction band. In this respect, in 2019 Cherifi *et al.* [69] conducted a computational study based on DFT methods to investigate the Cis-bis(isothiocyanato)bis(2,2′-bipyridyl-4,4′-dicarboxylato)ruthenium(II) (N3) dye adsorption potential onto hexagonal $ZnTiO_3$ in different crystallographic planes. When compared to anatase TiO_2 and wurtzite ZnO, $ZnTiO_3$ exhibited higher adsorption energy, due to its higher electronic density, demonstrating that it has larger specific surface area. Additionally, they simulated the HOMO and LUMO energies of $ZnTiO_3$ with N3 dye adsorbed on different crystallographic planes, exposing desirable energy levels to decrease electron recombination and assure the electron injection into the semiconductor's conduction band. Even though the study was done with N3 dye, similar results could be expected with N719 dye; since both are ruthenium complexes, both chemisorb to the semiconductor surface through carboxylic groups and their HOMO/LUMO

energy levels are similar. Their study probes the potential of $ZnTiO_3$ to be used in DSSC with ruthenium complexes as dyes.

A year later, in 2020, Cherifi *et al*. [70] conducted a similar study on the adsorption energy of an organic dye onto the surface of $ZnTiO_3$. This second study was also made by DFT methods but instead of using a synthetic dye, they simulated organic dyes; triphenylamine-based dyes with different linkages. They simulated the absorption spectra of the dyes before and after adsorption on the $ZnTiO_3$, its light harvesting efficiency, adsorption energy and its energy level alignment with the redox couple and the conduction band edge of $ZnTiO_3$. One dye in specific showed superiority among the other dyes in terms of its adsorption to the $ZnTiO_3$ surface, charge transfer and future photovoltaic performance. This study probes the potential use of $ZnTiO_3$ as a photoanode in DSSC sensitized with an organic dye. In conjunction with the previous study, verify the prospect sensibilization of $ZnTiO_3$ with Ru-complexes dyes and organic dyes, for its application in DSSC.

In 2020, Sarkar *et al.* [71] synthesized hexagonal $ZnTiO_3$ by a surfactant- free hydrothermal route in the presence of urea. In their study they also prepared TiO_2 anatase nanoparticles for its comparison to $ZnTiO_3$. The structural characterization of $ZnTiO_3$ demonstrated that it is possible to obtain cubic phase at low temperatures, and by calcination at 600 °C the hexagonal phase is obtained. The $ZnTiO_3$ was employed as photocatalyst to degrade p-nitrophenol and it was later sensitized with a porphyrin dye. The $ZnTiO_3$ showed superior photocatalytic activity thanks to its enhanced electron-hole separation, which is due to the injection of electrons from the conduction band of Ti to the conduction band of Zn. The same principle of

enhanced electron hole separation can be successfully applied in DSSC, joined with an improved electron injection rate from the dye to the $ZnTiO_3$, in comparison to TiO_2. This research work further confirms the promising use of hexagonal $ZnTiO_3$ as photoanode material in DSSC.

2.1 Synthesis of $ZnTiO_3$

$ZnTiO_3$ has been synthesized by various methods, each one having its own advantages and disadvantages. Among all the routes for the synthesis of $ZnTiO_3$, sol-gel synthesis, even though requiring a final thermal treatment for the obtention of the crystalline structure, is the one that provides greater morphological control, while being a greener and simple synthesis method. In Table 1 are shown some reports on the sol-gel synthesis of $ZnTiO_3$, highlighting the particle size obtained, the thermal treatment temperature and the crystalline phase obtained.

Table 1. Sol-gel synthesis methods for the obtention of $ZnTiO_3$.

Thermal treatment temperature (°C)	Particle size obtained (nm)	Crystalline structure	Ref.
800 °C	200-300	Hexagonal (with anatase as side product)	[37]
N/A	60-80	Hexagonal + cubic	[39]
700 °C	12-20	Cubic	[42]
N/A	100	Cubic	[45]
800 °C	30-50	Hexagonal	[46]
700 °C	60-100	Hexagonal	[47]
800 °C	120-300	Hexagonal + cubic	[72]
650 °C	30-70	Hexagonal	[73]

Nonetheless, is possible to obtain nanoparticles of pure hexagonal phase by sol-gel methods, these synthetic routes are controlled by several factors such as the concentration of the initial precursors or the reaction atmosphere (some are carried out under N_2 atmosphere [42,46]. Furthermore, by adjusting the thermal treatment temperature is possible to obtain different crystalline phases of the TiO_2-ZnO compounds.

2.2 Incorporation of Au nanoparticles in DSSC

Among the efforts to further increase the device efficiency, there have been incorporated plasmonic nanoparticles, especially Au nanoparticles, into the structure of DSSC. In Table 2 are shown the photovoltaic parameters of some plasmonic

DSSC, demonstrating the enhancement on its performance when these are incorporated.

Table 2. Photovoltaic parameters of plasmonic DSSC. The first value corresponds to the reference DSSC without plasmonic nanoparticles.

Photo-anode	J_{sc} (mA cm^{-2})	V_{oc} (mV)	FF	Efficiency (η) (%)	Enhance-ment (%)	Ref.
TiO_2-Au	15.1-17.2	0.75-0.78	0.62-0.62	7.00-8.45	20.7%	[74]
TiO_2-Au	14.1-16.7	0.65-0.64	0.67-0.68	6.17-7.35	19%	[75]
TiO_2-Au	11.5-14.7	0.73-0.72	0.71-0.70	6.00-7.38	23%	[76]
TiO_2-Au	14.4-15.3	0.67-0.67	0.61-0.61	5.92-6.37	7.6%	[77]
ZnO-Au	17.3-20.7	0.70-0.72	0.61-0.62	7.50-8.91	18%	[78]
ZnO-Au	8.75-15.0	0.58-0.50	0.32-0.33	1.6-2.5	56%	[79]

In 2014, Chandler *et al.* [75] studied the influence of Au nanoparticles size and concentration on TiO_2-based DSSC using N719 dye and I_3^-/I^- electrolyte. They proved nanoparticle sizes ranging from 5 to 85 nm, and concentrations of 0.24 and 0.1 wt%. Their optical and electrical characterizations showed that the best performance was obtained with metallic nanoparticles in the size of 15-40 nm in concentrations of 0.1 to 0.25 %wt. The incorporation of this size of nanoparticles increased the device efficiency due to the near-field enhancement altogether with irradiating light far-fields. On the other hand, nanoparticles of 5 nm of diameter do not exhibit a benefit, leading to the supposition that the improved near-field is lost as plasmonic heat. In addition, nanoparticles of 85 nm produce the large scattering cross-section of the irradiating light, therefore producing minimum enhancement in

the device efficiency. Besides stating the contribution of Au nanoparticles on the J_{SC}, this study also proves the importance of the size and concentration control of the nanoparticles to obtain an enhancement.

In 2018, Villanueva-Cab *et al.* [80] fabricated and characterized plasmonic DSSC with photoanodes of TiO_2 decorated with Au nanoparticles and characterized them by its J-V curves and oxygen K-edge X-ray emission and absorption spectroscopic studies. By the last techniques, they were able to probe that the plasmonic nanoparticles interact with the occupied energy levels of TiO_2, causing an upward deviation of the valence band and a decrease in the band gap. Due to the photocharging effect induced by the Au nanoparticles, the quasi-Fermi level upshifted. On the other hand, the J_{SC} shows an opposite trend, displaying that the band gap diminution has a positive effect in the J_{SC}, while the benefit of free plasmon is minimum.

Although, metallic nanoparticles have not yet been incorporated into $ZnTiO_3$ photoanodes for DSSC, some similar advances in the field of photocatalysis have been made.

In 2018, Reddy *et al.* [81] in the search for better photocatalysts synthesized Au-decorated $ZnTiO_3$ nanostructures. By sol-gel autocombustion method they synthesized hexagonal $ZnTiO_3$ and decorated them with Au nanoparticles by precipitation-deposition method. The incorporation of Au was done in 0.5%, 1% and 1.5% to evaluate its effect on the photocatalytic hydrogen production and, the results exhibited the best behavior with 1% of Au nanoparticles, with an efficiency of 7.14%. The boost in the production of hydrogen was attributed to the enhanced visible light

responsiveness of the material and the reduced electron hole recombination due to the LSPR of the metallic nanoparticles. Since a reduced electron hole recombination is also desired in DSSC, the decoration of $ZnTiO_3$ with Au nanoparticles is a promising alternative for device enhancement.

2.3 Critical analysis

The suitable band-gap energy, conduction band position and high electron mobility of hexagonal $ZnTiO_3$ make it a promising alternative to traditional DSSC photoanode materials. Furthermore, theoretical studies endorse the chemisorption of ruthenium-based dye complexes as well as organic dyes into its surface, demonstrating it as a better alternative to TiO_2 and ZnO. The application of $ZnTiO_3$ as photoanode in DSSC has only been reported once, however, further photovoltaic, and electrochemical analyses are required to properly characterize the behavior of this material in the DSSC.

Even though, it has been proved that the integration of Au nanoparticles into a photoanode of DSSC results in an efficiency enhancement of up to 20%, its incorporation onto $ZnTiO_3$ has not yet been reported for its use as photoanode in DSSC.

2.4 Scientific input

A DSSC based on a photoanode composed of hexagonal $ZnTiO_3$, both bare and Au-decorated, which reduces the electron recombination due to the fast electron transport of the $ZnTiO_3$. On the other hand, the Au nanoparticles promote the photon absorption due to its LSPR, while the photocharging effect increases the electron density of the semiconductor and shifts its Fermi level, improving the device performance.

2.5 Hypothesis

The incorporation of Au nanoparticles in the photoanode of a DSSC based on $ZnTiO_3$ nanoparticles enhances its efficiency.

2.6 Objectives and goals

- **General objective**
    - To compare the energy conversion efficiency of a DSSC with a photoanode composed of bare and Au-decorated hexagonal $ZnTiO_3$.
- **Specific objectives**
    - To synthesize ≤ 50 nm hexagonal $ZnTiO_3$ by sol-gel method.
    - To determine the hexagonal crystalline structure by X-ray diffraction (XRD), and Raman spectroscopy, the band-gap energy by Diffuse Reflectance Spectroscopy (DRS), the morphology by Field-emission

Scanning Electron Microscope (FE-SEM) and specific surface area by N_2 adsorption/desorption isotherms.

- To prepare pastes of hexagonal $ZnTiO_3$.
- To deposit a coating of the semiconductors on FTO by screen-printing and by mechanical profilometry measure the obtention of the desired thickness (5 μm).
- To determine the amount of N719 dye adsorbed on the hexagonal $ZnTiO_3$ by UV-Vis spectroscopy.
- To decorate the hexagonal $ZnTiO_3$ with Au nanoparticles varying its concentration.
- To determine the morphology of the Au-decorated $ZnTiO_3$ by FE-SEM, its band-gap energy by DRS, its elemental composition by Inductively Coupled Plasma Atomic Emission Spectroscopy (ICP-OES) and its emission and excitation spectra by photoluminescense (PL) spectroscopy.
- To prepare pastes of Au-decorated hexagonal $ZnTiO_3$.
- To deposit a coating of the Au-decorated $ZnTiO_3$ of 5 μm on FTO (screen-printing and mechanical profilometry).
- To assemble a DSSC with a photoanode of Au-decorated and bare $ZnTiO_3$ and characterize it by the obtention of its current-voltage curves, electrochemical impedance spectroscopy (EIS) and external quantum efficiency (EQE).

CHAPTER 3

METHODOLOGY

3.1 Synthesis of $ZnTiO_3$

The sol-gel synthesis of $ZnTiO_3$ started by mixing 1.58 mL of acetic acid (CH_3CO_2H, Sigma Aldrich, ≥99%) and 2.55 mL of tetrabutyl titanate ($Ti(OCH_2CH_2CH_2CH_3)_4$, Sigma Aldrich, 97%) under vigorous stirring for 10 min. Next, 5 mL of a 1 mol/L HCl solution were added dropwise with continued stirring. The solution was vigorously stirred and heated at 50 °C until the formation of a light-yellow sol. Afterwards, 2.23 g of zinc nitrate ($Zn(NO_3)_2 \cdot 6H_2O$, Sigma Aldrich, 98%) were added to the solution. For the samples **W-600** and **W-700** the $Zn(NO_3)_2 \cdot 6H_2O$ was dissolved in 3 mL of deionized water, while for the samples **WO-600** and **WO-700** the $Zn(NO_3)_2 \cdot 6H_2O$ was not dissolved. The solution was stirred and heated at 50 °C until the obtention of a whitish gel. The gel was dried at 340 °C for 2 h to eliminate the solvents. The dried gel was grounded into a fine powder and thermally treated at temperatures of 600 and 700 °C for 2 h with a heating ramp of 5 °C/min.

3.1.1 Decreasing of precursors' concentration

A second set of experiments was done decreasing the concentration of Zn and Ti precursors, while the solvent quantity was the same. The previously done procedure was performed, but the concentrations were reduced at 50% (sample **W2-50**) and 75% (sample **W2-75**). Therefore, for the synthesis at 50%, 0.79 mL of acetic acid (CH_3CO_2H, Sigma Aldrich, ≥99%) was mixed with 1.27 mL of tetrabutyl titanate ($Ti(OCH_2CH_2CH_2CH_3)_4$, Sigma Aldrich, 97%), next 5 mL of a 0.5 mol/L HCl solution were added, and finally, 1.11 g of zinc nitrate ($Zn(NO_3)_2 \cdot 6H_2O$, Sigma Aldrich, 98%) were dissolved in 3 mL of deionized water and incorporated into the previous mixture. Moreover, for the synthesis at 75% of precursors' concentration, 1.18 mL of acetic acid, 1.91 mL of tetrabutyl titanate, 5 mL of a 0.75 mol/L HCl solution and 1.67 g of zinc nitrate were used. Both samples, **W2-50** and **W2-75,** were dried at 340 °C for 1 h to obtain a dry gel, and subsequently treated at 600 °C for 2 h, with a heating ramp of 5 °C/min. Table 3 shows the samples' name and its synthesis specifications.

Table 3. Synthesis specifications of the samples.

Sample	Thermal treatment temperature (°C)	$Zn(NO_3)_2$ dissolved
W-700	700	Yes
WO-700	700	No
W-600	600	Yes
WO-600	600	No
W2-50	600	Yes
W2-75	600	Yes

3.2 Characterization of $ZnTiO_3$

The obtained $ZnTiO_3$ was first characterized by X-ray diffraction (XRD) to determine its crystalline structure. The analysis was performed with a Bruker D2 Phaser powder diffractometer within Bragg angle 2θ from 5 to 80 ° with Cu K λ radiation (1.5405 Å). The crystallite size was estimated with the data obtained from the XRD patterns and the Scherrer equation (Eq. 12).

$$\tau = \frac{K\,\lambda}{\beta\,cos\theta} \qquad \text{Eq. 12}$$

Where τ is the mean size of the crystallites, K is a dimensionless shape factor (0.94), λ corresponds to the wavelength of the X-ray radiation, β is the line broadening at half the maximum intensity and the Bragg angle is θ. The crystalline structure was further confirmed by Raman spectroscopy using a DRX Raman Microscope Class I (Thermo Scientific, USA) equipped with a 10x magnification microscope (Olympus M Plan, NA = 0.25) in back- scattered configuration. An argon ion laser operating at 532 nm and 180 mW was used as the excitation source. Field-emission scanning electron microscopy (FE-SEM) was used to examine the morphology using a FEI Nova NanoSEM 200 microscope with an accelerating voltage of 15 kV using a Helix detector in low vacuum mode. The specific surface area of the samples was determined by N_2 adsorption/desorption isotherms using a TriStar II Plus (Micromeritics) surface area analyzer at 77 K. The specific surface areas and pore sizes were determined using the Brunauer-Emmett-Teller (BET) and Barret- Joyner-Halenda (BJH) method, respectively. The band gap energy was calculated through the Kubelka-Munk function using the data from the diffuse reflectance spectra

(DRS). The DRS spectra was obtained with a UV–Vis NIR spectrophotometer Cary 5000 with an integration sphere.

3.3 Decoration of $ZnTiO_3$ with Au nanoparticles

The $ZnTiO_3$ was decorated by the in-situ synthesis of Au nanoparticles. A determined amount of $ZnTiO_3$ powder was dispersed in a 0.25 mmol/L hydrogen tetrachloroaurate trihydrate ($HAuCl_4 \cdot 3H_2O$ Sigma Aldrich, ≥99%) solution and it was heated until boiling. Once boiling, a determined amount of a 1 wt/v % sodium citrate dihydrate ($Na_3C_6H_5O_7 \cdot 2H_2O$ ≥, FG, Sigma Aldrich, 99%) solution was additioned, and the dispersion was stirred for 20 min. The resulting dispersion was centrifuged and rinsed with distilled water and dried at 100 °C for 2 h [14]. The $ZnTiO_3$ nanostructures were decorated with three concentrations of Au nanoparticles.

3.4 Au-decorated $ZnTiO_3$ characterization

The morphology of the Au-decorated $ZnTiO_3$ was obtained by FE-SEM using a FEI Nova NanoSEM 200 microscope with an accelerating voltage of 15 kV using a Helix detector in low vacuum mode. The elemental composition was estimated by EDXS using an INCA X-Sight EDS detector. The band gap energy of the composites was calculated through the DRS spectra (obtained with a UV–Vis NIR spectrophotometer Cary 5000 coupled with an integration sphere) and the Kubelka-Munk function. To quantify the concentration of Au, inductively coupled plasma-optical emission

spectroscopy (ICP-OES) was carried-out in a Thermo Electron-ICAP 6500. The samples were prepared by dissolving 21 mg of each sample in 12 mL of aqua regia (HCl/HNO_3-3:1). The acid digestion process was carried out in a hot plate (70−85 °C) using an open vessel. The excitation and emission spectra of the samples were obtained by PL spectroscopy using a fluorescence spectrophotometer Cary Eclipse using an excitation source of 270 nm.

3.5 $ZnTiO_3$ paste

To prepare the paste the $ZnTiO_3$ will be mixed with ethanol, terpineol (mixture of isomers, anhydrous, Sigma Aldrich, 99.5%) and ethylcellulose (100 cP, Sigma Aldrich). First, a solution of ethylcellulose 10 wt % was prepared with ethanol as solvent. This solution was added to a round bottomed flask containing the $ZnTiO_3$ and terpineol. The mixture was vigorously stirred with a magnet tip before remotion of ethanol using a hot-plate and continuous stirring. The same procedure was followed for the preparation of the pastes of both commercial TiO_2 and ZnO and Au-decorated $ZnTiO_3$.

3.6 Counter electrode preparation

The cathode was a platinum coated FTO. Platisol T (Solaronix) was applied dropwise on the FTO. To activate the platinum, the FTO was thermally treated at 450 °C for 30 min in air atmosphere [82].

3.7 Solar cell assembly

The DSSC based on $ZnTiO_3$ and Au-decorated $ZnTiO_3$ was assembled following the same procedure. The FTO substrates were washed in ultrasonic baths of deionized water, acetone and isopropanol for 10 min. The paste was deposited onto FTO by screen-printing method with a thickness of 11 μm, followed by a thermal treatment at 400 °C for 1 h. The photoanode was submerged in a 0.3 mM N719 ethanolic solution for 24 h. Next, they were rinsed with ethanol to eliminate any unabsorbed dye. Thereafter, a sandwich configuration was assembled using the counter electrode and photoanode and they were sealed together using a 60 μm-thick hot-melt film (Surlyn, DuPont) and applying heat. Finally, the electrolyte Iodolyte HI-30 (Solaronix) was injected through drilled holes in the counter electrode, and those holes were sealed with Surlyn and glass. The DSSC were made three times to evaluate the reproducibility. In Figure 6 is shown a schematic representation of a DSSC with a photoanode of $ZnTiO_3$/Au nanostructures.

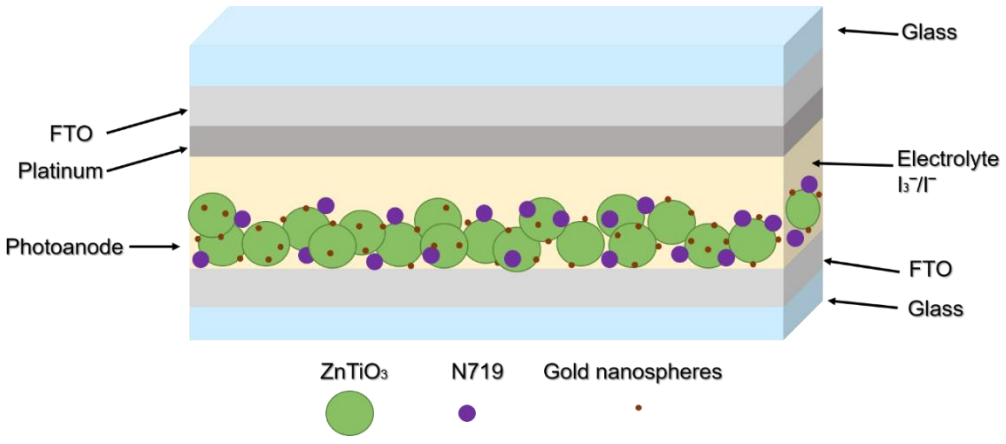

Figure 6. Schematic representation of a DSSC with a photoanode of $ZnTiO_3$/Au nanostructures.

In the Table 4 is shown the DSSC that will be assembled specifying the semiconductor material, the incorporation of Au nanoparticles and the sample name.

Table 4. DSSC photoanodes composition and its sample names.

Sample name	Photoanode	Au NP
Bare	$ZnTiO_3$	No
1% Au NPs	$ZnTiO_3$	Yes
0.5% Au NPs	$ZnTiO_3$	Yes
0.25% Au NPs	$ZnTiO_3$	Yes

3.8 Quantification of N719 dye adsorbed

After screen-printing the semiconductor paste and thermally treating the photoanodes, they were immersed in N719 solution for different times. To compare the dye loading capacity of the $ZnTiO_3$ to traditional DSSC photoanode materials the amount of chemisorbed dye molecules was quantified.

The sensitized photoanode was immersed in a 0.1 M NaOH solution for 20 min to desorb the dye. The obtained solution was analyzed in a UV-Vis spectrometer (Mettler Toledo UV5 spectrophotometer) and, applying the Lambert-Beer law the amount of N719 dye was calculated [83]:

$$A=\varepsilon\, c\, l \qquad \text{Eq. 13}$$

where A is the intensity of the UV–Vis absorption spectra at the maximum absorption peak of N719 (515 nm), ε is the molar extinction coefficient of the dye (14,100

$M^{-1}cm^{-1}$), c is the molecular concentration of the analyte, and l is the path length of the light beam [30].

3.9 Solar cell characterization

The DSSC based on $ZnTiO_3$, and its Au-decorated counterparts were characterized following the same procedure. The solar cells were tested in a solar simulator (Newport, Oriel Instruments, 91160 A) with a source meter (Keithley 2400) using a Xenon lamp as light source. Subsequently, with the current-voltage (J-V) curves obtained, the fill factor (FF) and efficiency (η) was determined using the following equations [84]:

$$FF = \frac{V_{MP} I_{MP}}{V_{OC} I_{SC}} \quad \text{Eq.14}$$

$$\eta = \frac{V_{OC} J_{SC} FF}{P_{in}} \quad \text{Eq. 15}$$

where V_{MP} is the voltage at maximum power, P_{in} is the input power, I_{MP} is the current at maximum power, V_{OC} is the open-circuit voltage, and J_{SC} is the short-circuit current.

EIS spectra were obtained with a potentiostat/galvanostat using a VMP3 Potentiostat/Galvanostat. The EIS spectra were recorded from 100 kHz to 5 Hz with an AC amplitude of 500 µA. EIS measurements were performed at open-circuit potential, and the light intensity was varied between 28, 50, 75 and 100 mW/cm^2. The results were analyzed and fitted using ZView software.

3.10 Waste Disposal

The disposal of the wastes generated during this project was done in accordance with the norms of the Facultad de Ciencias Químicas of the UANL. In the Table 5 are shown the generated residues and its disposal container.

Table 5. Waste disposal generated during this project.

Residue	Container
$ZnTiO_3$	B
Au-$ZnTiO_3$	F
$HAuCl_4$	F
FTO	Glass
Terpineol/ethanol	C

CHAPTER 4

RESULTS AND DISCUSSION

4.1 Sol-gel synthesis of $ZnTiO_3$

In the sol-gel synthesis method there are three fundamental steps: the hydrolysis, the condensation and the polymerization or chain growth [47]. Multiple parameters must be carefully controlled during these steps to assure the obtention of the desired compound, including the precursors concentration, catalyzers, pH and temperature, to mention some. Specially in the sol-gel synthesis of nanoparticles, the pH plays a fundamental role, it is well known a high pH is preferred [85]. At high pH the polymerization of the precursors is more branched or distorted, which produces smaller particles. Nonetheless, we are synthesizing a mixed oxide where a pre-hydrolysis is required. Since the precursors have a different hydrolysis rate, the gelation can take place at different times, producing phase separation. To overcome this problem, a catalyzer is added to enhance the hydrolysis rate of the less reactive

precursor [48]. Hence, in our synthesis HCl is added as a catalyzer for the hydrolysis of the titanium butoxide, and the pH of our system is 0.3.

4.2 X-ray diffraction (XRD)

After being dried and grounded the obtained powders were thermally treated in a muffle furnace at 600 and 700 °C.

During the thermal treatment the gel goes through a series of transformations; between 180 and 320 °C the physically bounded solvent desorbs and the organic acid decomposes, between 340 to 420 °C the Ti-OH in the polymeric matrix transforms to TiO_2 and between 420 and 480 °C the $Zn(NO_3)_2$ decomposes to form ZnO. With further temperature increase, above 600 °C, the TiO_6 octahedra and the ZnO_4 tetrahedra forming the TiO_2 and ZnO respectively, suffer an atomic rearrangement to form $ZnTiO_3$ [37,46,73].

In the Figure 7 are shown the XRD patterns of the samples **W-600** and **W-700**, synthesized with $Zn(NO_3)_2$ dissolved in deionized water, while in the Figure 8 are shown the XRD patterns of the samples **WO-600** and **WO-700**, synthesized with undissolved $Zn(NO_3)_2$. In both figures the JCPDS card No. 26-1500, corresponding to the hexagonal phase of $ZnTiO_3$ is shown. The four samples agree with the hexagonal phase of $ZnTiO_3$, where all the planes present in the JCPDS card can be indexed as seen in Figure 6. The four patterns show high crystallization and no preferential growth. Additional peaks, non-correspondent to hexagonal $ZnTiO_3$, at 25.33° and 30.69° are observed in all the samples. These signals correspond to the plane (101) of TiO_2 in anatase phase (JCPDS card No. 21-1272) and to the plane

(220) of the cubic phase of $ZnTiO_3$ (JCPDS card No. 39-0190) respectively. These minor impurities can be attributed to a small substoichiometric rate between the Ti and Zn precursors. Nonetheless, these signals are minimum, and the predominant phase is hexagonal $ZnTiO_3$.

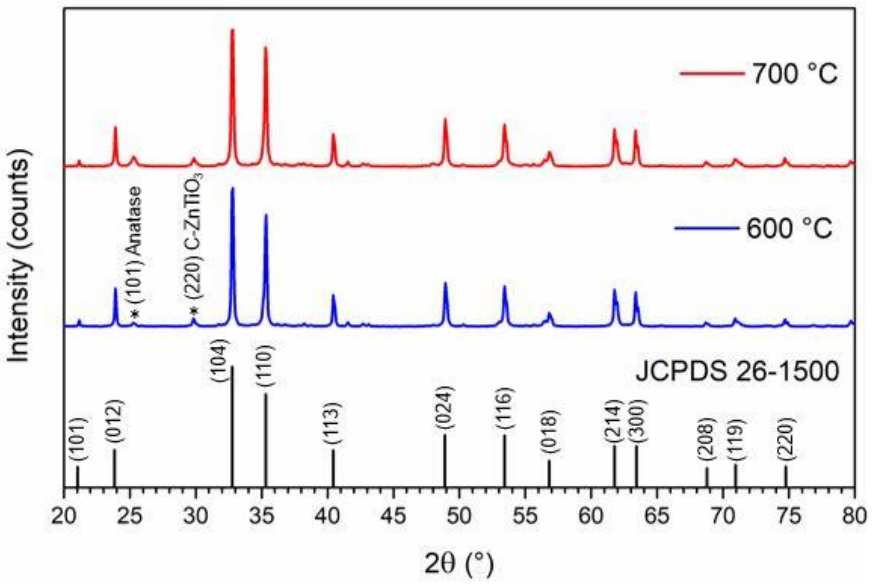

Figure 7. XRD patterns of samples **W-700** (700 °C) and **W-600** (600 °C), synthesized with dissolved $Zn(NO_3)_2$ and JCPDS card No. 26-1500.

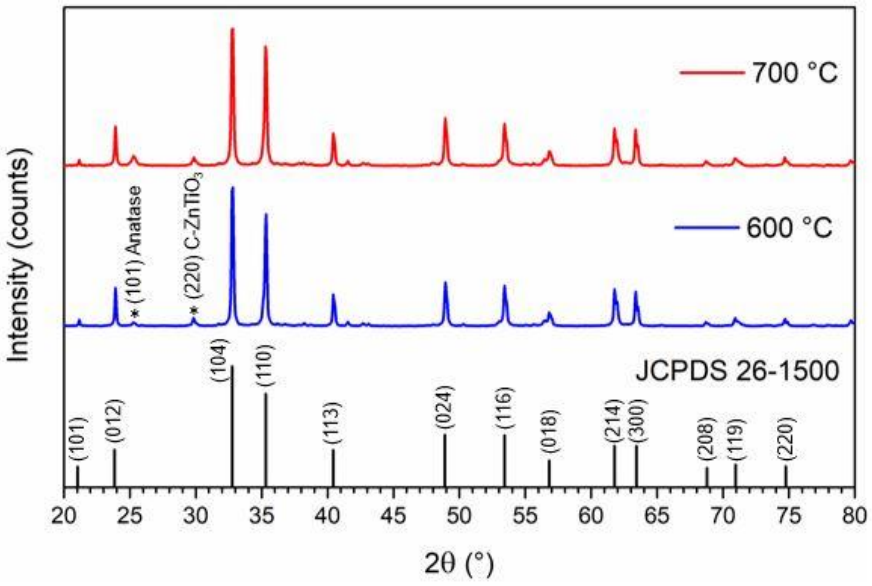

Figure 8. XRD patterns of samples **WO-700** (700 °C) and **WO-700** (600 °C), synthesized with undissolved $Zn(NO_3)_2$ and JCPDS card No. 26-1500.

Additionally, the crystallite size was estimated through the Scherrer equation (Eq. 12) and the results are shown in the Table 6. The crystallite size was obtained using the data of the principal peaks at 32.86°, 35.33° and 48.93° corresponding to the planes (104), (110) and (024) respectively, and the values shown are the average.

As can be observed the dissolution of $Zn(NO_3)_2$ does not exerts a great influence in the growth of the crystallites, but the increase in the thermal treatment temperature does. As the temperature is increased from 600 to 700 °C a minor growth in the crystallite size is obtained. Therefore, it can be assumed that a 600 °C the $ZnTiO_3$ crystals are formed, but as the temperature increases, they continue to grow.

Table 6. Crystallite size and synthesis specifications of samples **W-600**, **W-700**, **WO-600** and **WO-700**.

Sample	Crystallite size (nm)	Dissolved Zn precursor	Thermal treatment temperature (°C)
W-700	44.86	Yes	700
WO-700	45.43	No	700
W-600	41.41	Yes	600
WO-600	42.17	No	600

Based on the XRD results, the estimated crystallite size and minor thermal treatment temperature, the samples **W-600** and **WO-600** were selected for further characterization.

4.3 Raman spectroscopy

To confirm the XRD results, the Raman spectra of the samples WO-600 and W-600 were collected. According to literature, $ZnTiO_3$ possess 10 Raman active modes in accordance with its group theory (C_{3i}). As observed in Figure 9, the Raman vibrations detected at 142, 230, 390, 468 and 615 cm^{-1} can be assigned as E_g symmetrical phonon modes, while the vibrations detected at 175, 264, 342, 482 and 708 cm^{-1} can be assigned as A_g symmetrical phonon modes.

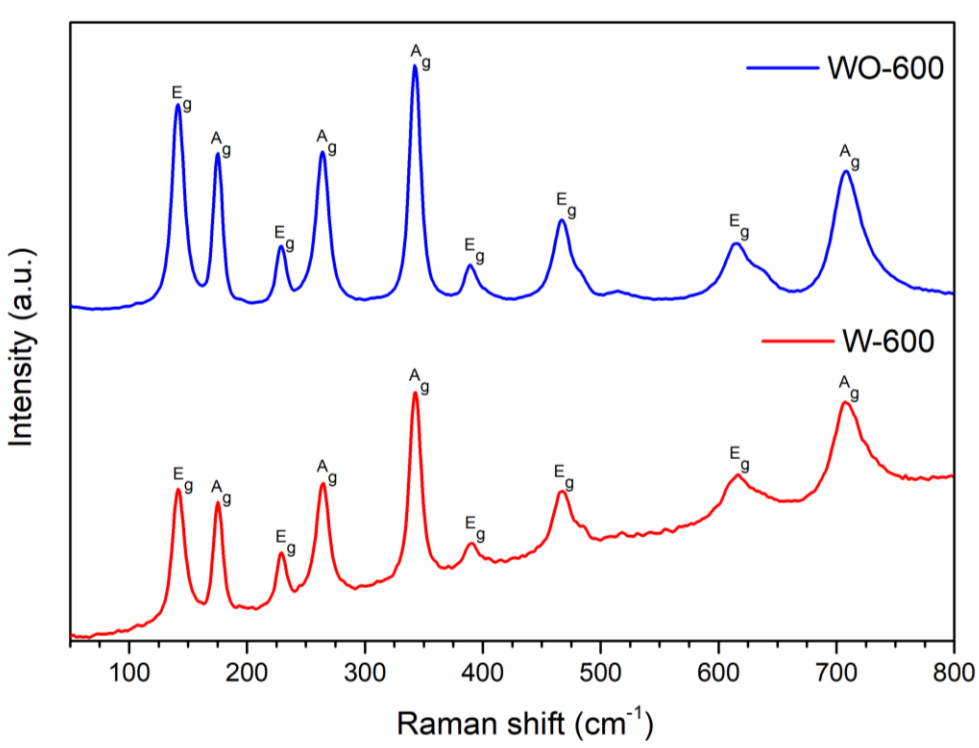

Figure 9. Raman spectra of samples WO-600 and W-600.

In Fig. 10 the deconvolution of the signals at 468 and 482 cm^{-1} is shown. These signals are overlapped due to its proximity and the low intensity of the Ag mode at 468 cm^{-1}. The deconvolution was done in Origin 8 software using Lorentz functions obtaining a fit between 0.91 and 0.98. Overall, the Raman results agree with those previously reported for hexagonal $ZnTiO_3$ [86–88], confirming the obtention and purity of both samples. It is important to note that the sample WO-600 exhibits a more intense signal and the absence of photoluminescence denoting a higher degree of crystallization.

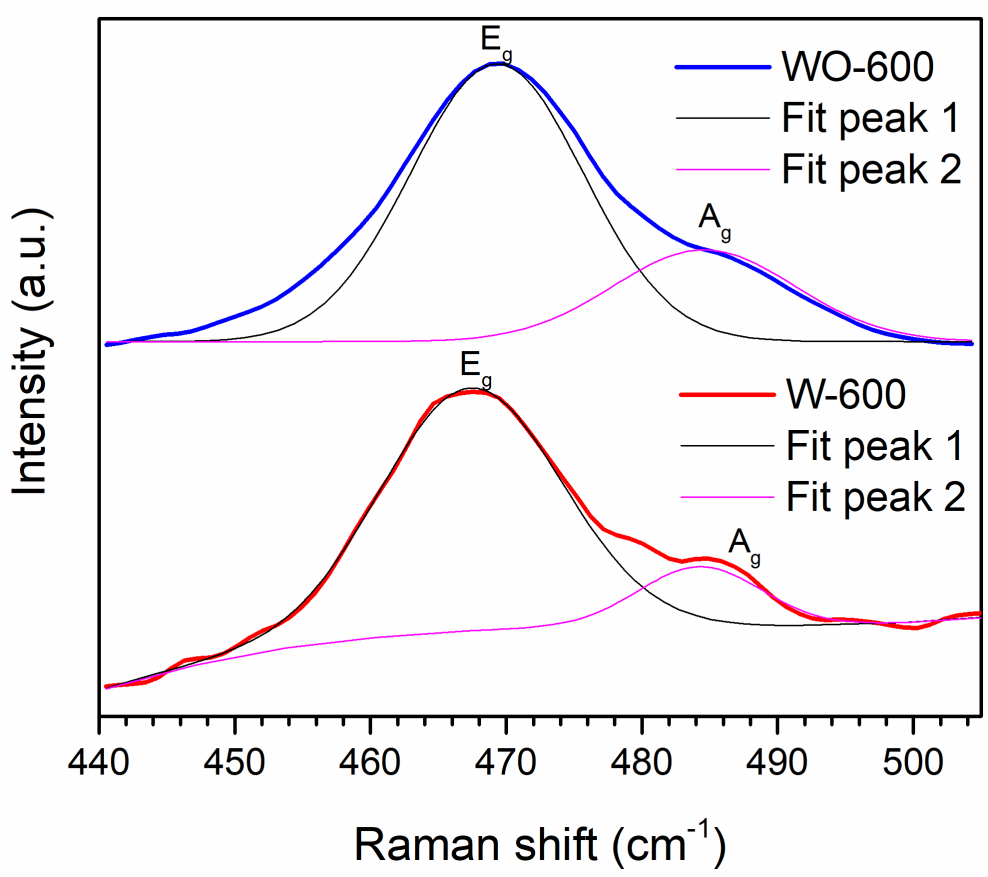

Figure 10. Deconvolution of signals at 468 and 482 cm^{-1} of samples WO-600 and W-600

4.4 Field emission scanning electron microscopy (FE-SEM)

The Figure 11 exhibits the FE-SEM images of samples W-600 and WO-600. A statistical particle size analysis was carried out using ImageJ software (developed at the National Institutes of Health (NIH-USA, Java-based public domain, freely available)) and the data of 130 particles. The estimated particle sizes are 62.2 ± 28.2 nm and 39.2 ± 9.8 nm for the sample W-600 and WO-600, respectively. As observed, the dissolution of the zinc precursor exerts a great influence in the particle size, even

though the crystallite size is very similar. The change in particle size and its dispersity can be attributed to the difference in the concentration of hydroxy ions between the two synthesis methods (with $Zn(NO_3)_2$ dissolved and undissolved). Since the complex $Ti(OBu^n)_3OAc$ possess organic ligands that are not easy hydrolyzed, the local densification of the titanium atoms is forbidden, thus the polymerization is delayed [89]. As a result, swollen branched heterometallic polymeric chains are formed during gelation, which are known to form smaller particles [47].

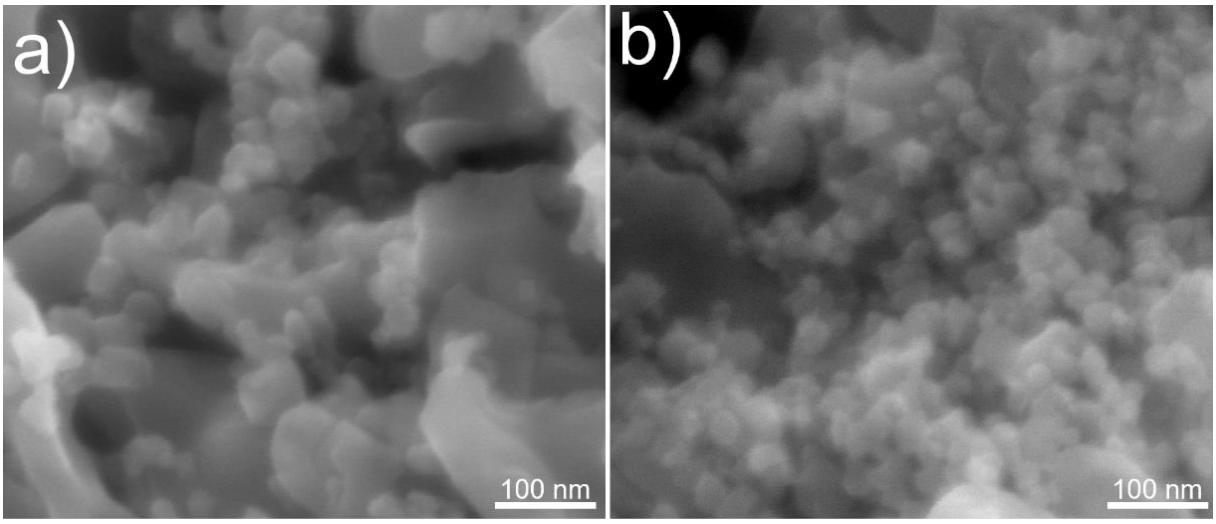

Figure 11. FE-SEM micrographs of samples a) W-600 and b) WO-600.

4.5 Diffuse reflectance spectroscopy (DRS)

To determine the optical band gap energy of the $ZnTiO_3$ samples their DRS spectra were collected. Figure 12 shows the DRS spectrum for the indirect band gap semiconductors W-600 and WO-600, and the Figure 13 displays the Tauc plot ($[F(R)hv]^{1/2}$ vs. photon energy).

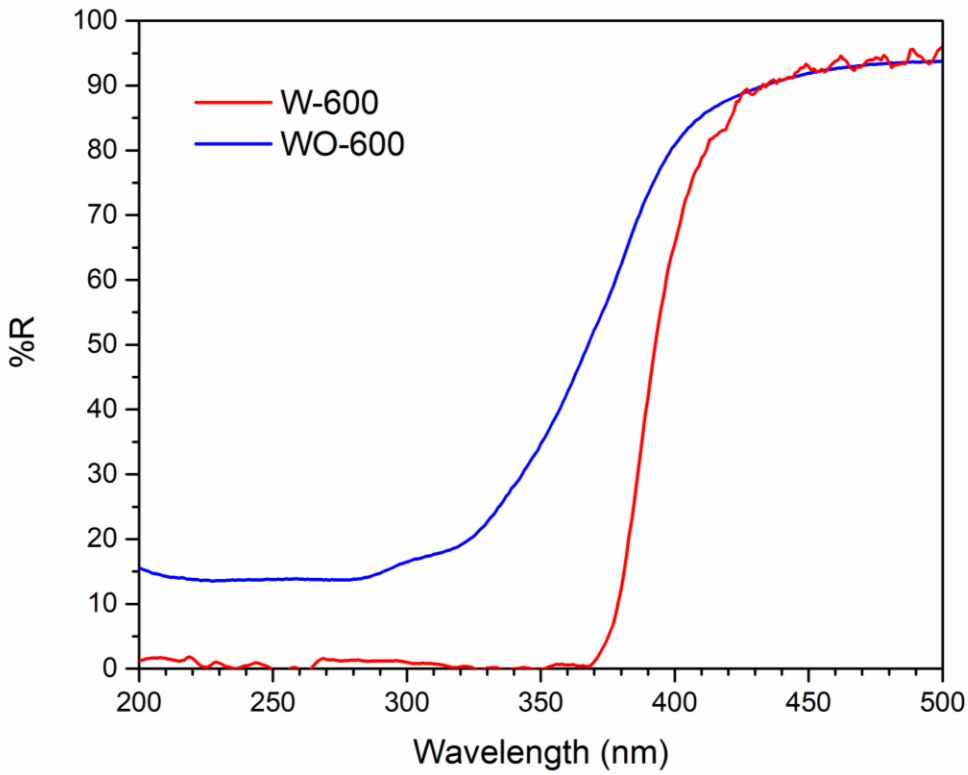

Figure 12. Reflectance spectra of samples W-600 and WO-600.

The calculated optical band gap energies are 3.24 and 3.08 eV for samples W-600 and WO-600, respectively, values that agree with those previously reported for $ZnTiO_3$ structures [69,90,91]. The difference in the band gap energy between the two samples could be attributed to their variation in particle size and crystallization degree, as observed in the Raman spectra, XRD and FE-SEM micrographs. For DSSC photoanode materials a narrow band gap is preferred to benefit the charge separation and transport, thus the sample WO-600 would be favored for this application.

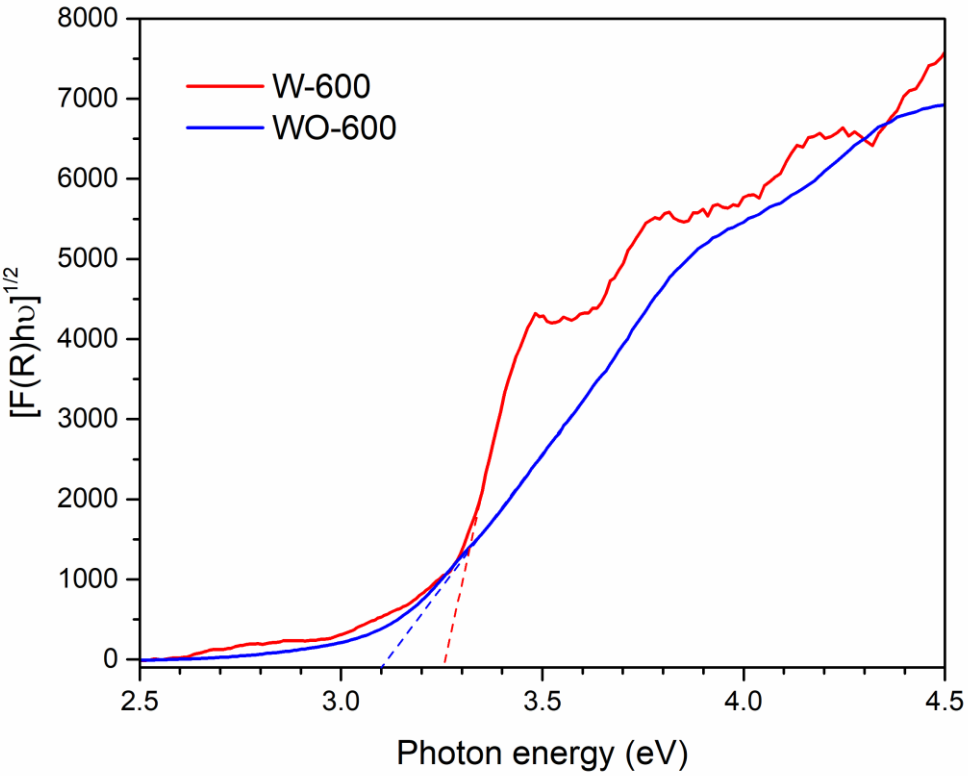

Figure 13. Tauc plots of samples W-600 and WO-600.

4.6 N_2 physisorption analysis

In Figure 14 and Figure 15 are shown the N_2 adsorption-desorption isotherms at 77 K for samples W-600 and WO-600, respectively. Moreover, the estimated pore size distribution obtained by the BJH method is presented in Figures 16 and 17. Both isotherms can be classified as type IV isotherms with a H1 type hysteresis loop, according to the IUPAC classification [40], characteristic of mesoporous structures with cylindrical pores. The BET surface areas are 12.72 m^2/g and 13.96 m^2/g for the samples W-600 and WO-600 respectively, while the pore width ranges between 2

and 10 nm for both samples. The difference in surface areas can be attributed to the diminution in the particle size, since smaller nanoparticles provide larger surface area, which agree with the FE-SEM results.

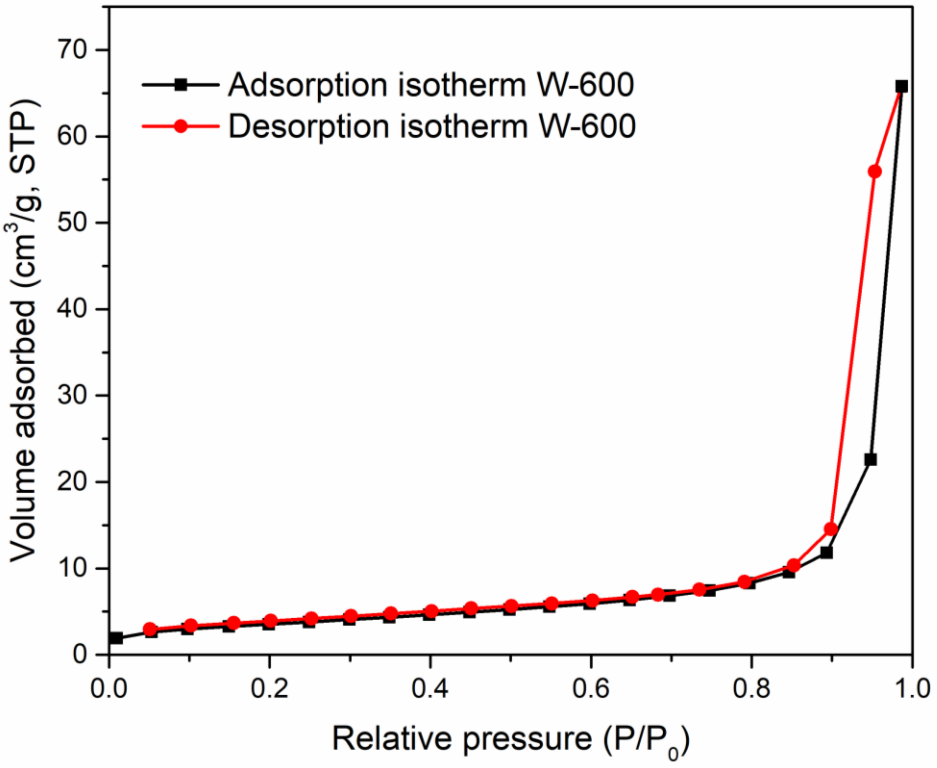

Figure 14. N_2 adsorption-desorption isotherms of sample W-600.

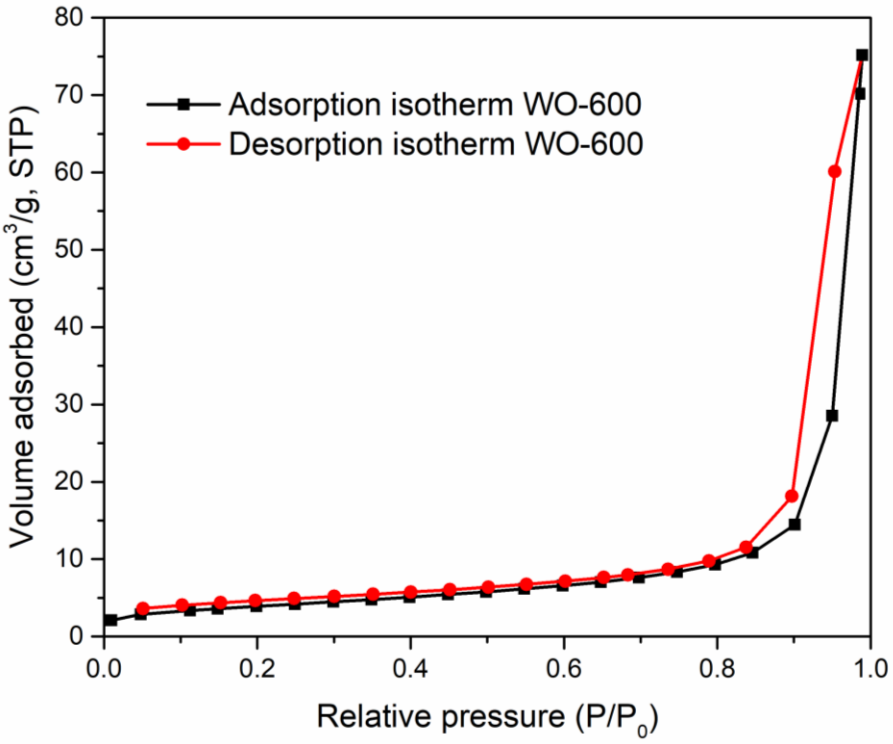

Figure 15. N_2 adsorption-desorption isotherms of sample WO-600

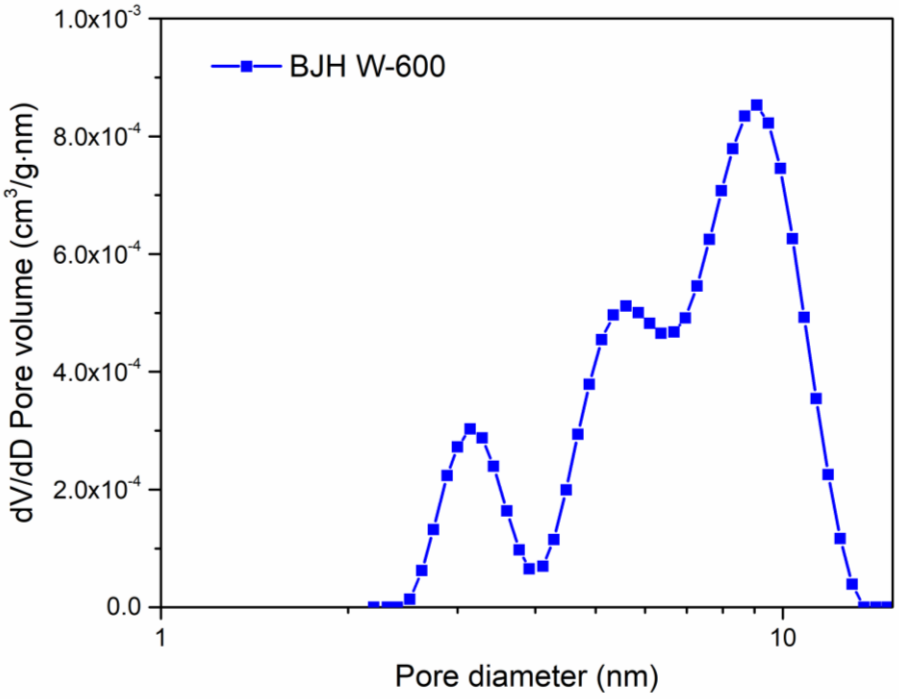

Figure 16. BJH pore size distribution of sample W-600.

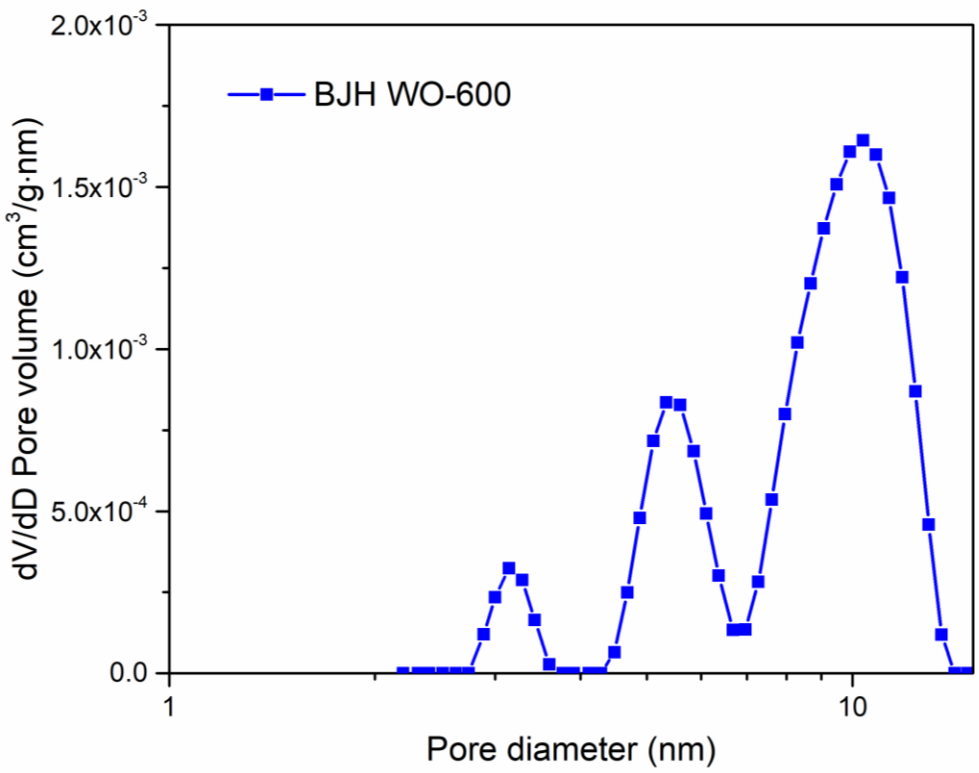

Figure 17. BJH pore size distribution of sample WO-600.

For its application as DSSC photoanode materials, the semiconductors must possess a high surface area, to allow more dye chemisorption, and be mesoporous, in other words they should have pores ranging between 2 to 50 nm [92]. The mesoporosity of the semiconductor allows the diffusion of the electrolyte throughout the photoanode coating, thus yielding a high dye regeneration rate [93]. According to the N_2 physisorption results, both samples comply with these requirements. Nonetheless, further analyses must be conducted to determine the best one for this application, especially the sample yielding higher dye loading.

4.7 Dye loading capacity

To determine the concentration of N719 adsorbed on samples W-600 and WO-600, coatings of 5 μm were deposited by screen-printing technique over glass substrates and immersed in N719 ethanolic solution for 3, 6, 12, 24 and 30 h. Next, the concentration of adsorbed N719 was calculated using the procedure explained in the Methodology section. Table 7 shows the molar concentration of N719 detached from each coating, where it is observed that the maximum dye adsorption is obtained within 24 of immersion for both samples. No further increase in dye loading is observed at longer immersion times, so it can be inferred that at 24 h all the available sites for dye anchoring have bonded with N719 molecules.

Table 7. Dye adsorption of N719 on photoanodes W-600 and WO-600 at different sensitization times.

Sample	Immersion time (h)	Dye adsorption (nmol/cm^2)
W-600	3	22 ± 3.6
W-600	6	33 ± 0.64
W-600	24	35 ± 8.1
W-600	30	39 ± 2.9
WO-600	3	44 ± 1.7
WO-600	6	71 ± 8.3
WO-600	24	93 ± 4.3
WO-600	30	91 ± 7.2

The chemisorption of N719 molecules onto the semiconductor surface is done by a combination of bidentate-bridging and H-bonding between its carboxylic groups and Metal-O bonds of the semiconductors surface [69,94]. In Figure 18 is shown the UV-Vis absorption spectra of N719 adsorbed on both samples after 24 h, including its standard deviation for reducibility. Both spectra exhibit the characteristic absorption bands of N719 at 376 and 515 nm, although the signal of the sample WO-600 is considerably enhanced due to its superior dye loading. As shown on Table 7 at 24 h of immersion time, the sample WO-600 attains an adsorption 165% superior to that of sample W-600. These results agree with FE-SEM and N_2 physisorption analysis, given that smaller particles provide larger surface area, thus increasing the availability of anchoring sites. These results reveal that the N719 dye loading capacity of sample WO-600 is comparable to that of TiO_2 nanoparticles, reassuring the promising application of $ZnTiO_3$ nanoparticles as photoanode material for DSSC [95–98].

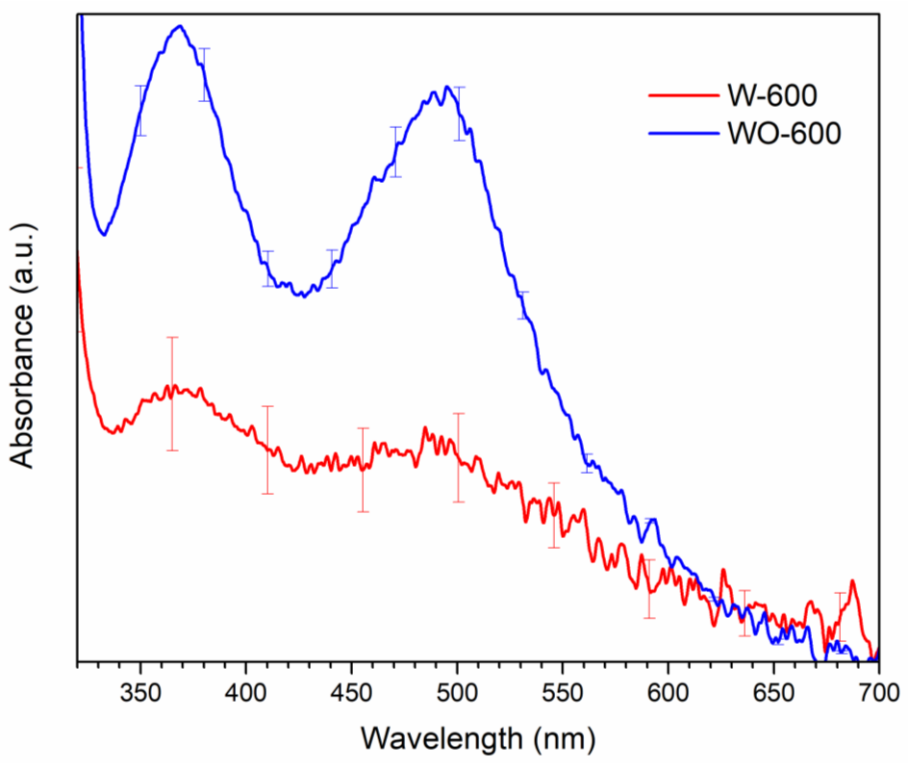

Figure 18. UV–Vis absorption spectra of N719 adsorbed on W-600 and WO-600 photoanodes sensibilized for 24 h with standard deviation.

In Table 8 are shown the synthesis specifications, crystallite size, particle size, band gap energy, specific surface area and dye concentration adsorbed in 24 h. Due to its dye adsorption capacities, band gap energy and particle size, the sample WO-600 was selected for the next stage of this work.

Table 8. Synthesis specifications, crystallite size, specific surface area, nanoparticle size, and band gap energy of samples W-600 and WO-600.

Sample	$Zn(NO_3)_2$ dissolved	Thermal treatment temp (°C)	Crystallite size (nm)	Particle size (nm)	Band gap energy (eV)	Specific surface area (m^2/g)	Dye adsorbed in 24 h ($nmol/cm^2$)
W-600	Yes	600	41.41	62.2 ± 28.2	3.24	12.72	35 ± 8.1
WO-600	No	600	42.17	39.2 ± 9.8	3.08	13.96	93 ± 4.3

The second step of this work consisted in the incorporation of Au nanoparticles into the semiconductor nanostructure for later incorporation into DSSC photoanodes. This incorporation has been done by decorating the surface of the $ZnTiO_3$ nanoparticles using the citrate reduction method, as further described in the Methodology section. To study the effect of the Au nanoparticles concentration on the optoelectronic properties of the final composite, and the DSSC device performance, three different concentrations of Au have been tested.

4.8 Field emission scanning electron microscopy (FE-SEM) and Energy dispersive X-ray spectroscopy (EDXS)

The Au-decorated $ZnTiO_3$ nanoparticles were first characterized by FE-SEM to observe the morphology of the composites. As seen in Figure 19, 20 and 21, it is not possible to determine the presence or the morphology of the Au nanoparticles. This

poor visualization could be attributed to the limited concentration of the Au, as well as the electronic microscope resolution.

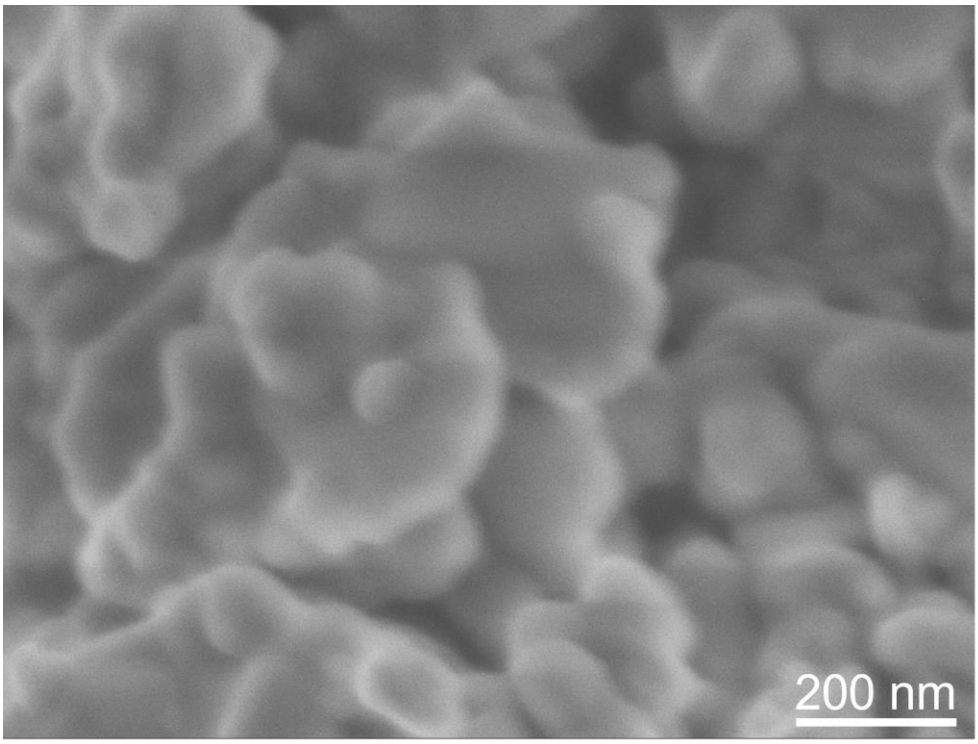

Figure 19. FE-SEM micrograph of $ZnTiO_3$ decorated with 1% Au NPs.

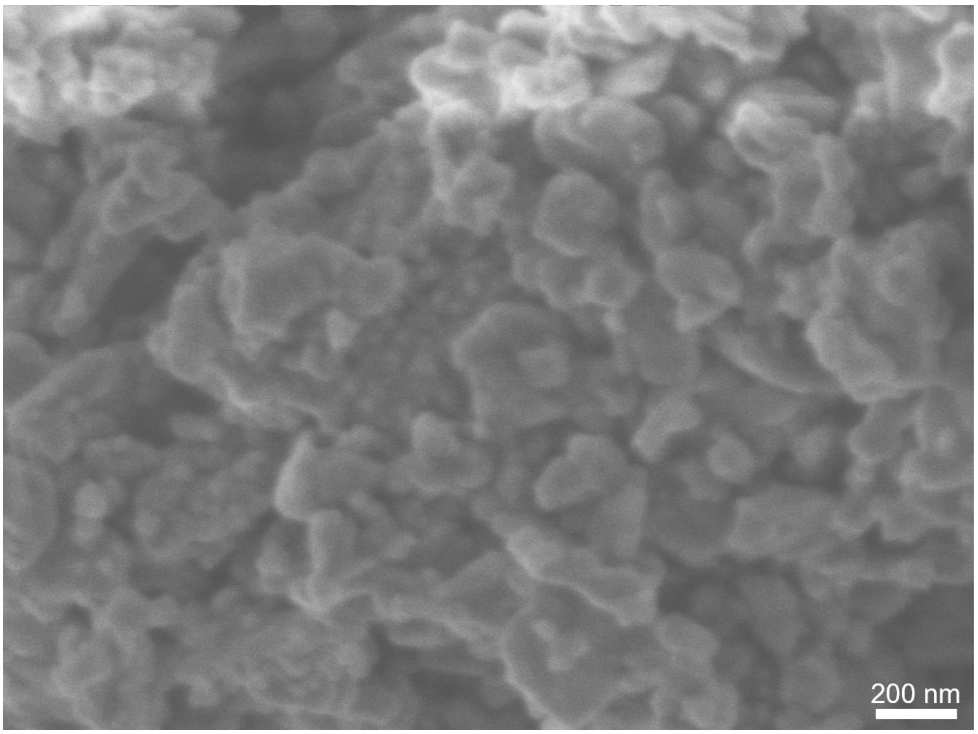

Figure 20. FE-SEM micrograph of $ZnTiO_3$ decorated with 0.5% Au NPs.

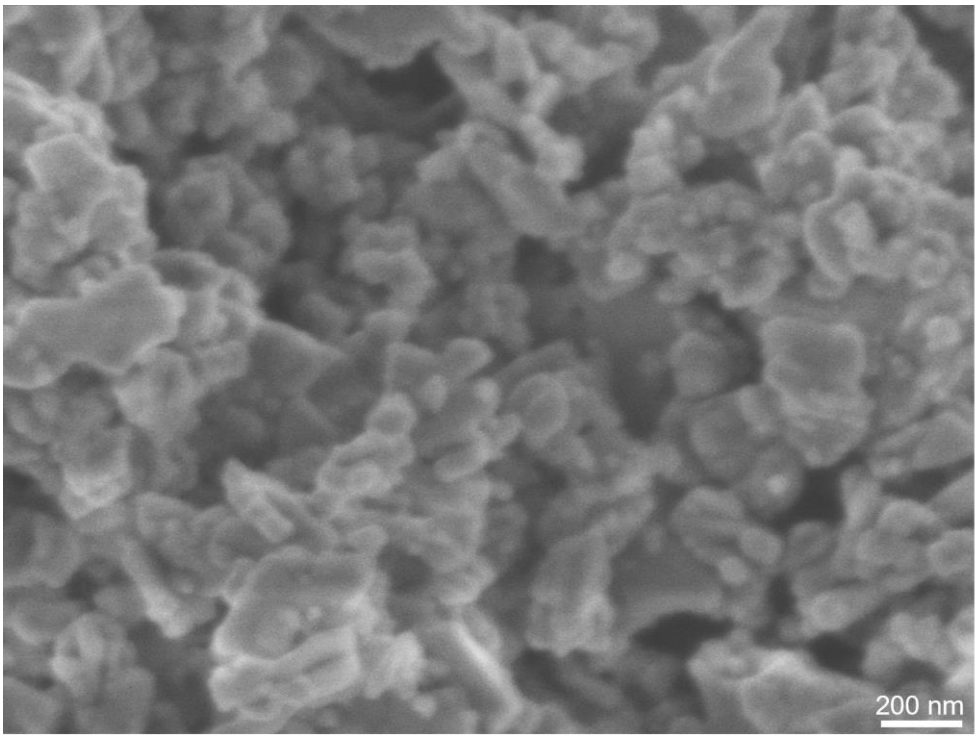

Figure 21. FE-SEM micrograph of $ZnTiO_3$ decorated with 0.25% Au NPs.

To corroborate the presence of Au in the samples the elemental composition was determined by EDXS analysis, and the spectra are shown in Figures 22, 23 and 24, corresponding to the samples decorated with 1%, 0.5% and 0.25% Au NP, respectively. The spectra present peaks corresponding to Zn, Ti, O, and Au, and no other peaks corresponding to impurities. The presence of Au can be determined by the peaks at 2.120 keV and 9.712 keV, corresponding to M and La valence shell, respectively. It is important to mention that as the concentration of Au decreases, also the intensity of the EDXS peaks decreases, due to the reduced presence of Au atoms in the sample surface.

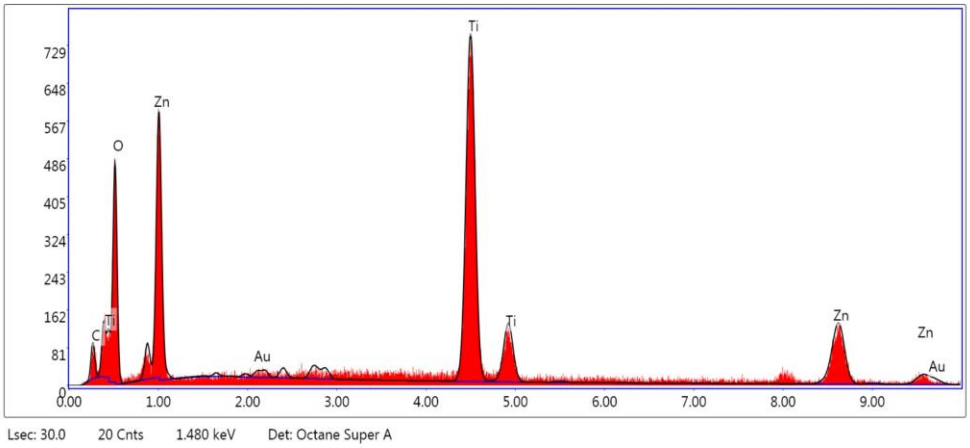

Figure 22. EDS spectrum of $ZnTiO_3$ decorated with 1% Au NPs.

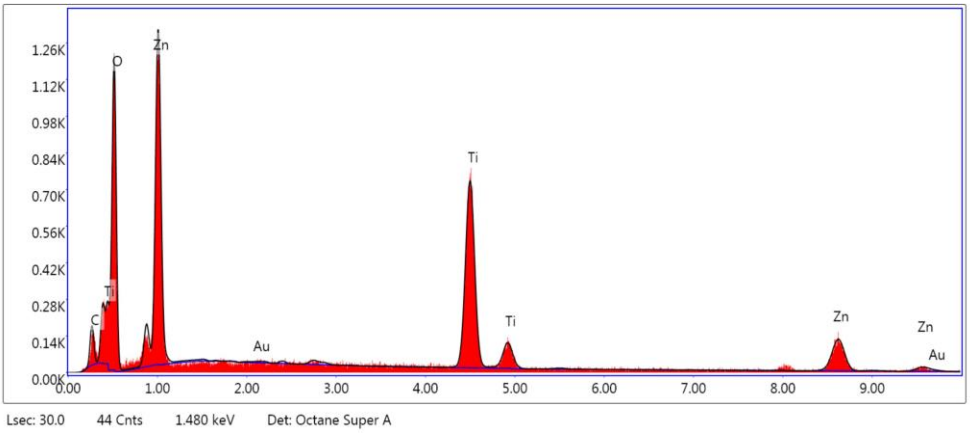

Figure 23. EDS spectrum of $ZnTiO_3$ decorated with 0.5% Au NPs.

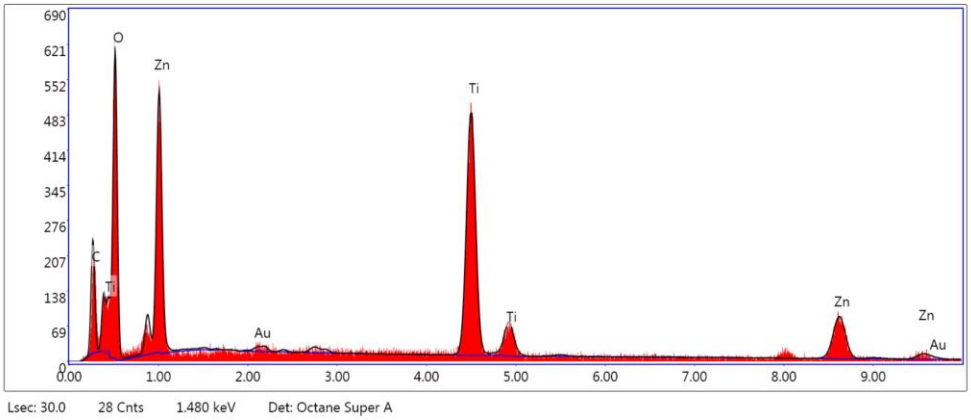

Figure 24. EDS spectrum of $ZnTiO_3$ decorated with 0.25% Au NPs.

The elemental mappings shown in Figures 25, 26 and 27 further corroborates the presence and diminution of the Au nanoparticles in accordance with the synthesis method. Even though the presence of Au nanoparticles cannot be seen in FE-SEM micrographs, the EDXS and the elemental mappings demonstrate its presence in all the samples, as well as its well distribution all over the sample surface.

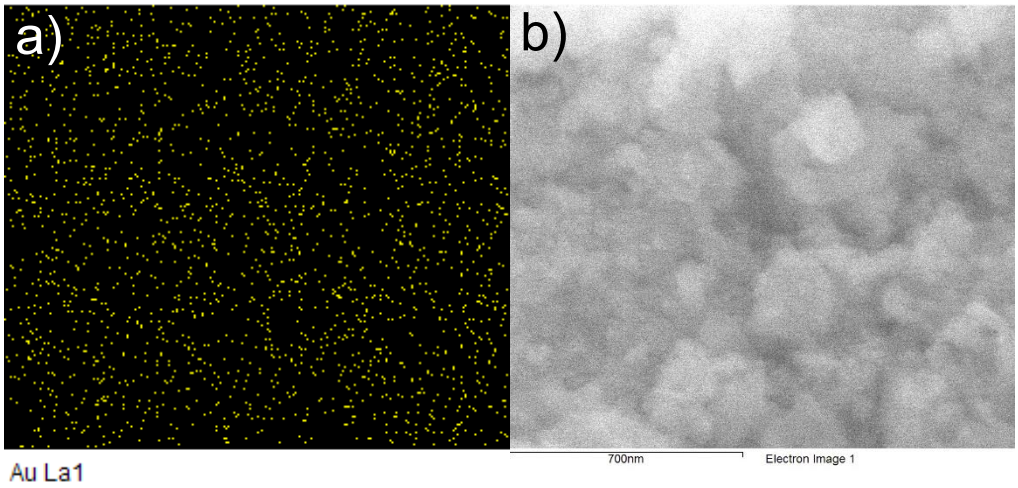

Figure 25. a) Au elemental mapping of $ZnTiO_3$ decorated with 1% Au NPs and b) the FE-SEM image from which the mapping was obtained.

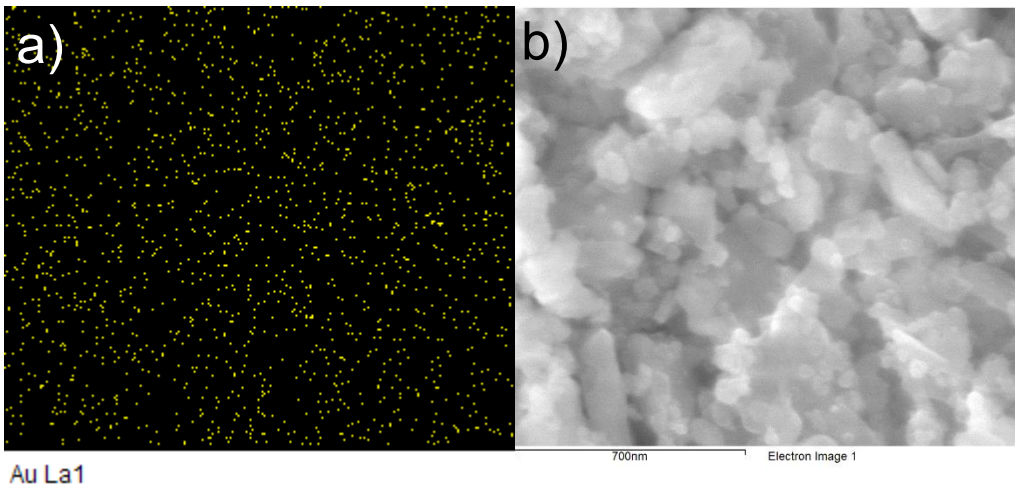

Figure 26. a) Au elemental mapping of $ZnTiO_3$ decorated with 0.5% Au NPs and b) the FE-SEM image from which the mapping was obtained.

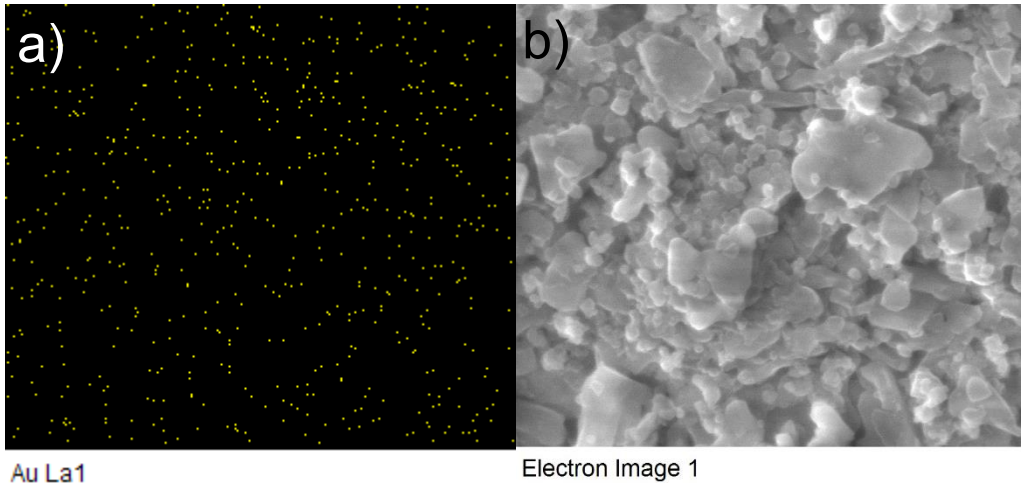

Figure 27. a) Au elemental mapping of $ZnTiO_3$ decorated with 0.25% Au NPs and b) the FE-SEM image from which the mapping was obtained

4.9 Inductively coupled plasma - optical emission spectrometry (ICP-OES)

Even though the EDXS characterization has confirmed the presence of Au in the samples we do not know its exact concentration since the reaction yield of the Au NPs synthesis is nowhere nearly 100% [99]. To determine the concentration of Au in each sample, a quantitatively analysis was conducted. By ICP-OES the ppm of Au in each sample was calculated as 3000, 1300 and 800, for the samples named 1%, 0.5% and 0.25%, respectively. These results are in accordance with those from EDXS, showing the minimal presence of Au in the composites.

Since it has been reported in literature that the incorporation of plasmonic nanoparticles into semiconductor nanostructures changes the optoelectronic properties of the bare materials, the next step was the optoelectronic characterization of the samples. The modulation of the optoelectronic properties has

been attributed to the coupling between the energy levels of the semiconductor and the plasmonic particles, driving the semiconductor's quasi-Fermi level to more negative potentials [80].

4.10 Diffuse reflectance spectroscopy (DRS)

The first optoelectronic property determined from the $ZnTiO_3$-Au nanoparticles was the band gap energy. To determine the band gap energy the DRS spectra, shown in Figure 28, was collected. The presence of Au can be further confirmed by its characteristic absorption band at 530 nm [100], which increases along the presence of Au. Another interesting phenomenon observed is that as the concentration of Au increases, the reflectance diminishes, hence the absorption is boosted. This can be ascribed to the LSPR of the Au nanoparticles, which is well known to improve the photon absorption due to the enhancement of the electric field near the particle surface [101].

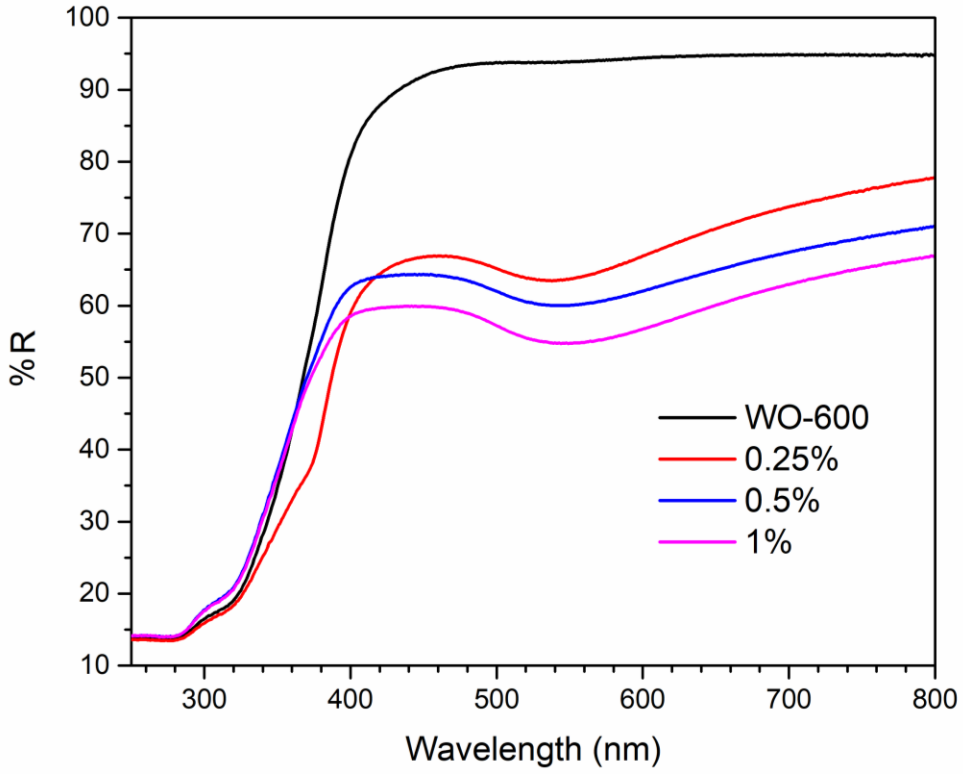

Figure 28. DRS spectra of Au-decorated $ZnTiO_3$ nanostructures.

The band gap energy of the composites was calculated using the Kubelka-Munk transformed, seen in Figure 28 and in Table 9 are shown the E_g values.

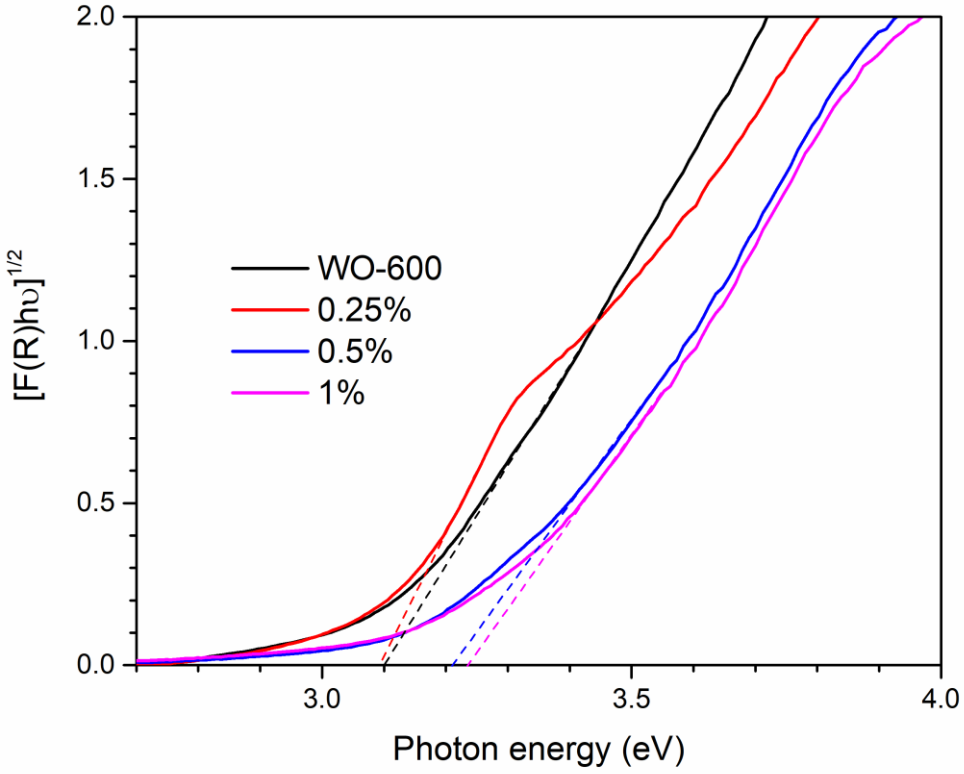

Figure 29. Tauc plot of Au-decorated $ZnTiO_3$ nanostructures.

As shown in Figure 29 the samples with 0.25% Au nanoparticles does not have a significant change in the band-gap energy. On the other hand, the samples with 0.5 and 1% Au nanoparticles exhibit a widening of their band-gap energy. This phenomenon has been reported in literature and has been ascribed to the Burnstein-Moss effect. The Burnstein-Moss effect describes how an apparent increase in the band-gap energy can occur when all the states close to the conduction band get occupied, therefore the absorption edge shifts to higher states. In accordance with

Pauli's exclusion principle these energy states cannot be occupies by another charge carrier, giving rise to a widening of the band-gap energy [102,103]. In our case, the states close to the conduction band can be occupied by hot electrons injected by the Au nanoparticles.

The difference in band-gap energy between the samples can be attributed a different Au particle size. A different particle size modifies the available energy states; thus, the Fermi level is adjusted [104]. Thus, the junction between semiconductor and Au nanoparticle shifts along with the Au Fermi level. As the concentration of Au was modified, also the Au precursor and sodium citrate reductor were adjusted, thus giving particles with different sizes due to the ratio of precursors in the reaction medium. This behavior has already been reported in literature [105].

Table 9. Band gap energy and Au ppm determined by ICP-OES of Au-decorated $ZnTiO_3$ samples.

Sample	Band gap energy (eV)	Au (ppm)
WO-600	3.10	0
1%	3.23	3000
0.5%	3.21	1300
0.25%	3.09	800

4.11 Photoluminescence spectroscopy (PL)

The next optoelectronic property characterized was the electron-hole recombination rate by PL spectroscopy, which spectra is shown in Figure 30. PL spectroscopy

detects the photoluminescense generated by a sample as it falls from the excited state to ground state [106–108]. Therefore, by measuring the PL spectrum is possible to determine the electronic band gap, and to observe the materials defects and impurities at photon energies below the band gap which can act as an electron trap [109]. As PL is not observed for metals, since they do not possess a band gap [107], the signals obtained for our Au decorated samples reflects the behavior induced by them in the $ZnTiO_3$.

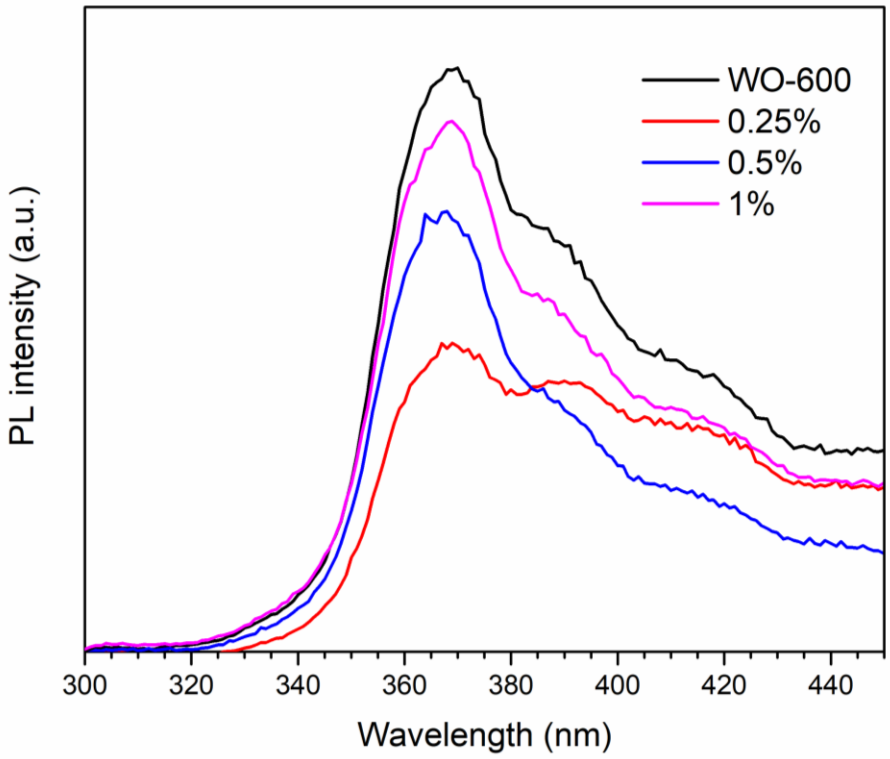

Figure 30. PL spectra of Au-decorated $ZnTiO_3$ samples.

As observed in the PL spectra, no tendency between the PL response and the Au concentration is observed. If we recall the synthesis of the Au nanoparticles, in the presence of $ZnTiO_3$, the sodium citrate reduces the Au, but it also reduces the

semiconductor surface by interacting with the oxygen atoms [105]. Therefore, when the concentration of Au is increased, more sodium citrate is added to the reaction medium, thus the composite recombination is also enhanced. The recombination is boosted because of the presence of oxygen vacancies on the materials' surface, hence undermining the effect of the recombination reduction of the Au. This phenomenon, previously reported with reduced GO [105], also explains the low synthesis yield of the Au nanoparticles.

As previously mentioned, the electronic band gap can also be calculated by PL using the highest peak intensity [110]. The electronic band gap of the bare $ZnTiO_3$ is 3.35 eV, while the optical band gap was calculated as 3.08 eV. The difference between the optical and electronic band gap has been identified as the exciton binding energy [111]. Therefore, the exciton binding energy of the bare sample is estimated as 0.27 eV. But what is the exciton binding energy? When a certain energy photon is absorbed by the material, an electron and a hole are formed, in the conduction and the valence band, respectively. These charges can be either an exciton or an electron-hole pair, being an exciton, a quasi-particle consisting of a tightly bounded electron and hole that move together, and an electron-hole pair free charge [110,111]. Thus, the required energy to dissolve the exciton, is the exciton binding energy.

As observed in Figure 30, various peaks at higher photon energies than the band gap can be found. These additional peaks or signals can be ascribed to intermediate electronic states belonging to defects in the crystalline structure, such as interstitial defects or oxygen vacancies [112,113]. Being the sample 0.5% Au NPs the one

which possess the smaller number of additional peaks; hence it can be inferred that is the one with less intermediate electronic states which can act as an electron trap.

All the samples were selected for the final stage of the work. Even though, the sample 0.25% Au NPs exhibits the minor recombination rate, the sample 1% Au NPs presents the major absorption, and the sample 0.5% Au NPs presents the minor amount of in-between electronic states. Consequently, to determine the best Au concentration for the selected application, it was decided to test all the samples.

Dye-sensitized solar cells with photoanodes of bare and Au-decorated $ZnTiO_3$

Due to the DRS and PL spectroscopy results it was decided to assemble DSSC with all the samples to determine the best composite for this application. The assembling details can be found on the Experimental section. In all the assembled solar cells the only component material varied was the photoanode, the sensitizer used was N719 dye, I_3^-/I^- was used as electrolyte and platinum was used as a counter electrode. In addition, a thickness of 5 μm was deposited for all the samples. It is important to mention that the reproducibility of DSSC was tested by assembling 3 identical devices for each sample.

4.12 Current-voltage (J-V) curves

The first photovoltaic characterization done to the DSSC was the obtention of the current-voltage curves. Through this characterization the basic photovoltaic

parameters of solar devices can be found, such as the V_{OC} and the J_{SC}. The V_{OC} represents the maximum voltage that may be extracted from the photovoltaic cell, and it can be determined by the x-axis on the J-V curve when there is no J_{SC}. Additionally, the J_{SC} is the maximum current that the solar cell than give and it can be determined on the y-axis when there is no voltage. With these two essential parameters the FF and the efficiency (η%) of the device can be calculated using the equations 14 and 15 [114,115]. The FF relates to the ideality of the solar cell, the closer to the unity, the more ideal the device is. Finally, the most known parameter of a solar cell is the efficiency, which is the relation between the light power irradiating the device and the power output of it [116].

In the Figure 31 are shown the most representative J-V curves of the assembled solar cells and the photovoltaic parameters of all the reproducible devices can be found in the Table 10. Evidently, the least efficient device is the one without Au NPs (bare) with an efficiency of 0.09%, and the most efficient device is the one decorated with 0.5% of Au NPs with an efficiency of 0.18%

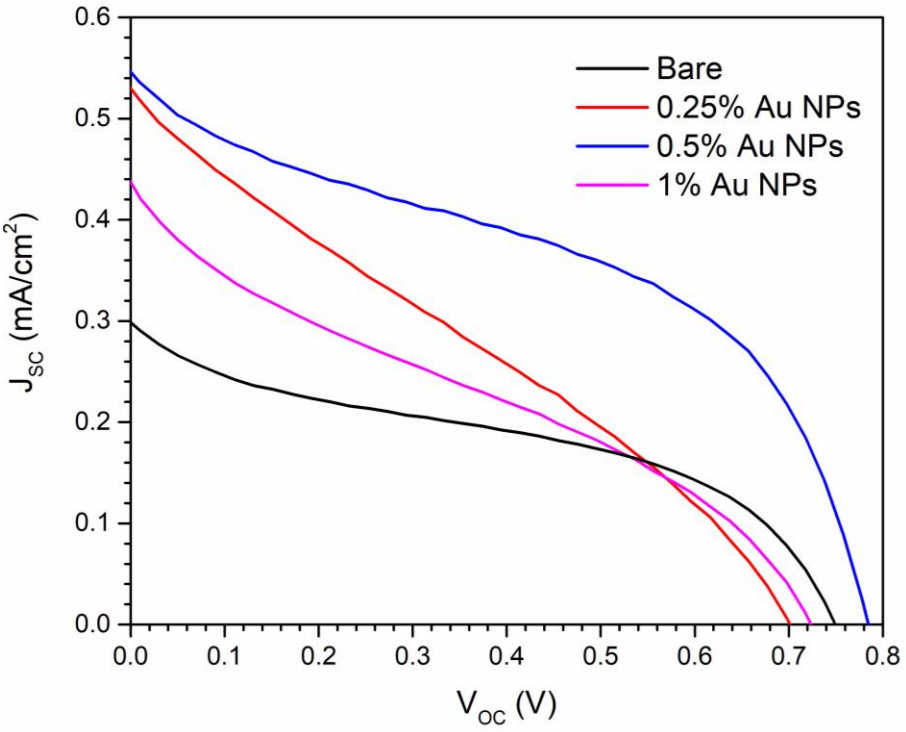

Figure 31. J-V curves of DSSC based on bare and Au decorated $ZnTiO_3$.

Table 10. Photovoltaic parameters of DSSC based on bare and Au decorated $ZnTiO_3$.

DSSC	V_{OC} (V)	J_{SC} (mA/cm^2)	FF	η%
Bare	0.63 ± 0.16	0.31 ± 0.02	0.4 ± 0.02	0.09 ± 0.01
0.25% Au NPs	0.72 ± 0.035	0.41 ± 0.16	0.33 ± 0.08	0.10 ± 0.009
0.5% Au NPs	**0.78 ± 0.009**	**0.5 ± 0.08**	**0.47 ± 0.04**	**0.18 ± 0.017**
1% Au NPs	0.76 ± 0.023	0.39 ± 0.07	0.34 ± 0.08	0.09 ± 0.001

Even though there does not exist a considerable difference in the efficiency of the samples bare, 0.25 and 1% Au NP, their photovoltaic parameters differ. Despite the devices with Au NPs exhibit larger V_{OC} and J_{SC}, their efficiency is largely affected by the low fill factor (FF). The enhancement of the V_{OC} can be ascribed to the photocharging effect supplied by the plasmonic nanoparticles, which increases the electronic density of the composite, thus conducting the semiconductor's Fermi level to more negative potentials [80]. This is important in DSSC because the V_{OC} is defined as the difference amid the redox level of the electrolyte and the semiconductor's Fermi level [117].

Moreover, the higher J_{SC} can be ascribed to the increased photon absorption promoted by the LSPR of the Au nanoparticles which boosts the dye excitation. The interaction between the incident light and the plasmonic nanoparticle gives rise to the local enhancement of electromagnetic fields, which are called "near-fields" due to its proximity to the metallic particle. This phenomenon occurs when the plasmonic nanoparticles act as light concentrators focusing the incident light into the particle surface, thus the dye molecules in the vicinity couple with the enhanced near-fields resulting in an increased electron-hole separation in the molecule [118,119].

In DSSC the J_{SC} is related with the quantity of dye molecules chemisorbed on the semiconductor's surface, the dye regeneration rate and the electron injection and collection efficiency [120]. Evidently, the DSSC based on $ZnTiO_3$ exhibits a much lower J_{SC} than DSSC based on TiO_2 previously reported in literature. This could be attributed to a lower injection rate from the LUMO of the dye to the $ZnTiO_3$ conduction band. Another factor which might be influencing the low J_{SC} is the probable instability

of $ZnTiO_3$ under acidic conditions, as it is the N719 ethanolic solution. This behavior has been widely reported for ZnO devices, where it has been proved that the electron injection is hindered by the formation of Zn^{2+}-dye complexes [121], and due to the nature of our semiconductor this could also be happening in the interface of the semiconductor and the dye.

Finally, the low (FF) can be ascribed to a high series resistance (R_S) and a low shunt resistance (R_{shunt}) [7,122]. The series resistance (R_S) does not affect the V_{OC}, however at values near the maximum power (P_{max}) its value is increased diminishing the FF [123]. The Rs is a combination of various internal resistances including the resistance of the conducting substrate, the resistance of the electron transfer at the interface of photoanode/electrolyte and the resistance of the external contacts. Generally, the Rs can be identified by the slope in the y-axis of the J-V curve [124]. Another resistance hindering the FF is the shunt resistance (R_{shunt}), which inversely to the Rs, increases the FF of a solar cell when its value is enhanced. The R_{shunt} can be identified by the slope in the x-axis of the J-V curve. A low R_{shunt} has been related to the leakage current (IDC), also called dark current, which is produced due to the back electron migration between the FTO substrate and the electrolyte [125]. This recombination hinders the current that can be extracted from the device and enhances the electron recombination. Therefore, it has been reported in literature the deposition of a TiO_2 compact layer on the FTO, over which the mesoporous layer of TiO_2 of deposited [125–127]. In our case we did not incorporate a compact layer because the incorporation of TiO_2 would block the electron transfer from the $ZnTiO_3$

due to the conduction band energy levels mismatch, causing a short circuit of the device [123].

4.13 Quantum efficiency

The second photovoltaic characterization done to the $ZnTiO_3$-based DSSC was the determination of the quantum efficiency (QE). The QE represents the number of photons of certain wavelength collected by the device that are transformed into electric current. The ideal QE has a square shape, as the FF, however it is reduced due to recombination effects [128]. The QE obtained for the assembled solar cells is shown in the Figure 32. These results are consisted with those obtained by the J-V curves, since they exhibit the same trend. It is observed that all the devices display a peak around 340-360 nm, which is consistent with the band gap energy of the composites and the bare semiconductor. It is important to remark that the absorption in this wavelength range increases along presence of Au nanoparticles, being the sample 0.5% the one that possess the highest QE. Another peak can be found in the range between 500 and 550 nm for all the samples. This peak can be attributed to two phenomena: to the N719 dye and the Au nanoparticles. The N719 dye presents its maximum absorption peak at 515 nm, however this signal increases simultaneously with the concentration Au nanoparticles. It is known that Au nanoparticles exhibit an absorption in the range of 520-550 nm [117,129,130], therefore its presence enhances and complements the absorption of the N719 dye due to its LSPR and its nanoantennae behavior as previously mentioned.

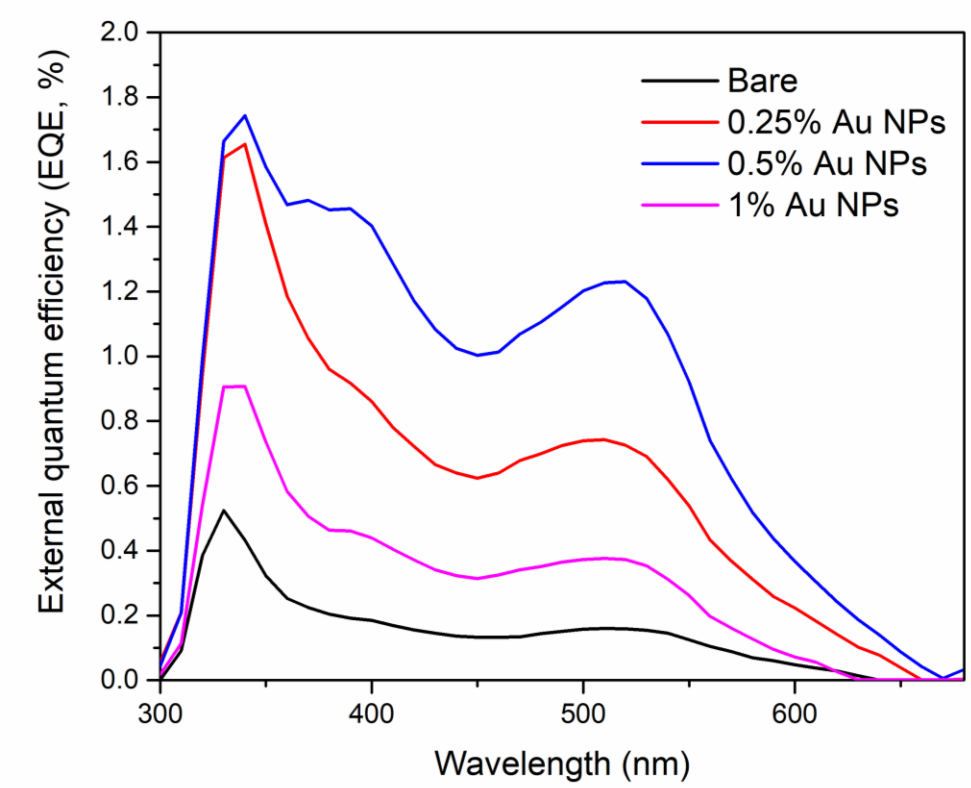

Figure 32. External quantum efficiency of DSSC based on bare and Au decorated $ZnTiO_3$.

4.14 Electrochemical impedance spectroscopy (EIS)

Even though the J-V curves and the QE provide fundamental information about the assembled devices, they cannot give information about the electron transport processes inside the DSSC. To investigate the electron transfer dynamics and to know the real reason behind the increased performance EIS was used. Through EIS, the Nyquist plots are obtained and using the software ZView and an equivalent circuit the data can be modeled to obtain the series resistance (R_S), chemical capacitance (C_μ), recombination resistance (R_{CT}), and electron lifetime (τ).

In TiO_2 DSSC the Nyquist plots show three semicircles; the high frequency one is ascribed to the charge transfer resistance in the counter electrode (R_{PT}), the second one is connected to the recombination resistance at the semiconductor-electrolyte interface (R_{CT}) and C_{μ}, and lastly the low frequency semicircle relates to the diffusion impedance in the redox mediator (R_d), although if I_3^-/I^- is used it is usually dismissed. And lastly, the displacement from the origin is associated with the R_s [131–133].

The EIS measurements were performed under four different light illuminations; 28, 50, 75 and 100 mA/cm^2 at open-circuit conditions, each one giving different V_{OC} values for the devices due to the modification of the quasi-Fermi level of the photoanode [134]. The data from the EIS spectra were analyzed using the software ZView and the results were fitted to the electrical circuit shown in Figure 33a. Normally, the equivalent circuit for the fitting of DSSC, shown in Figure 33b, is more complex. The equivalent circuit shown in Figure 33b has 3 different resistances, each correspondent to a semicircle in the Nyquist plot, as previously described. However, in our Nyquist plots only one semicircle is observed, thus the equivalent circuit had to be simplified to properly fit the results. The presence of only one semicircle in the Nyquist plot has been associated with an exponentially higher resistance at mid-frequencies, which overruns the lower resistance in higher frequencies, hence is not possible to differentiate between the R_{PT} and R_{CT} [135].

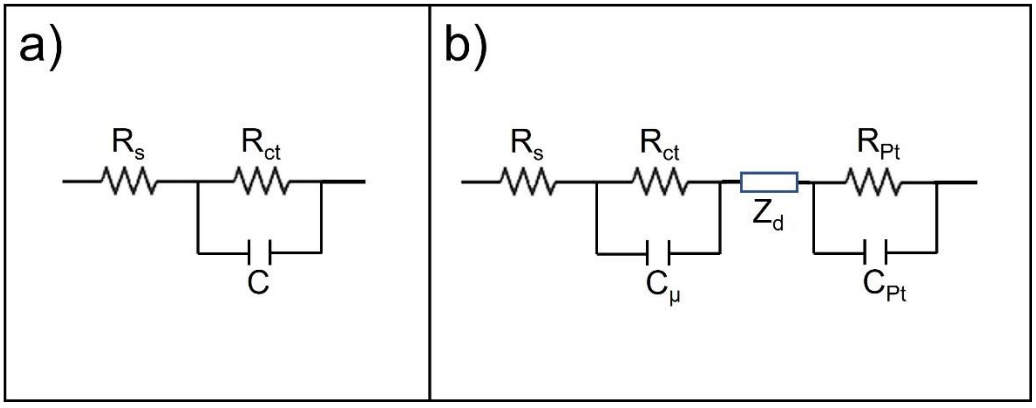

Figure 33. a) Equivalent circuit used to fit the EIS data and b) equivalent circuit reported in literature.

The Nyquist plots obtained under 1 sun (100 mA/cm^2) are shown in Figure 34. The Figure 34 demonstrates that the R_S effectively is diminished upon the incorporation of the Au nanoparticles, being the sample with 0.5% Au nanoparticles the one which possess the lowest one.

On the other hand, Figure 35 shows a zoom into the high frequency region to display the displacement from the origin, equal to the R_S of each DSSC. The R_S does not present a tendency; however, the bare sample exhibits the larger one.

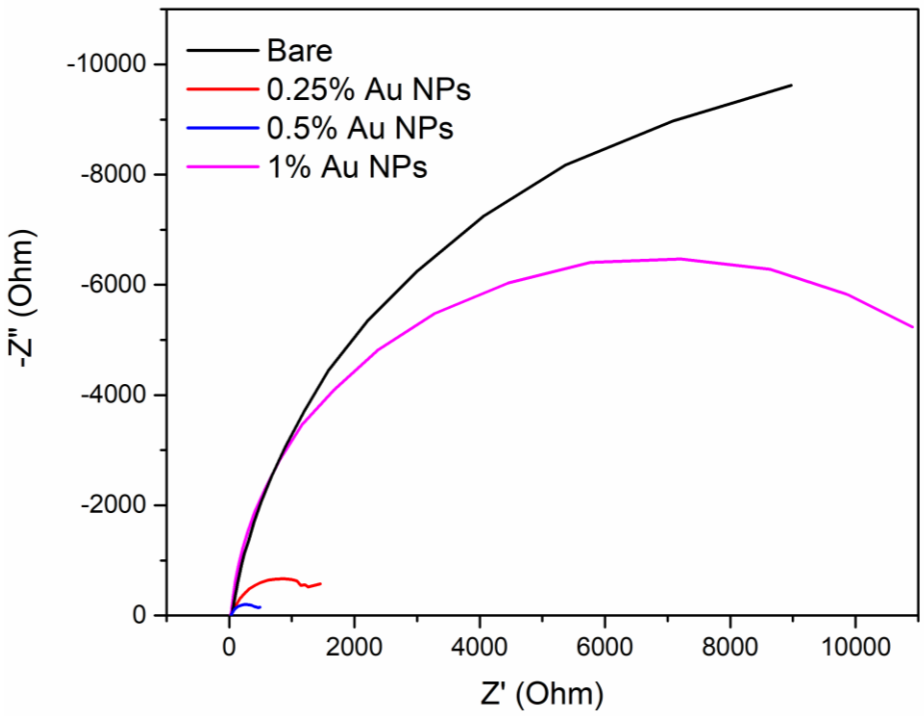

Figure 34. Nyquist plots of DSSC based on bare and Au decorated $ZnTiO_3$ under 1 sun illumination.

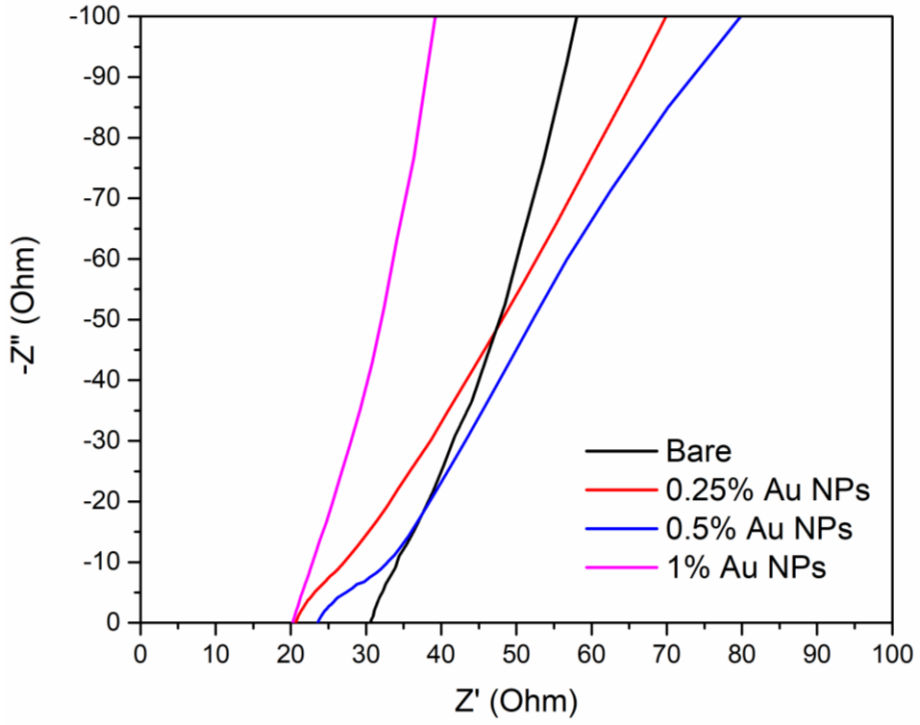

Figure 35. Nyquist plots of DSSC based on bare and Au decorated $ZnTiO_3$ under 1 sun illumination with close-up on high frequency.

The Figure 36 displays the C_μ as a function of the V_{OC}, and the results exhibit the normal exponential dependence which agrees with the exponential distribution of trap states, a, as given in equations 16 and 17 [14]:

$$C_\mu = C_0 exp\left(\frac{aqV_{OC}}{k_B T}\right) \quad \text{Eq. 16}$$

$$C_0 = \frac{q^2 N_T a}{k_B T} exp\left(-\frac{a(E_C - E_{redox)}}{k_B T}\right) \quad \text{Eq. 17}$$

Where N_T is the total density of traps, $(E_C - E_{redox)}$ is the position of the semiconductor's conduction band in relation with the redox energy of the electrolyte, T is the temperature, and k_B is the Boltzmann constant. Therefore, equation 16 and 17 demonstrate that the C_μ can be different for each of the composites since it is related with the trap distributions, which also explains the different slopes for the samples. The DSSC assembled with 1% Au NPs exhibits the lower C_μ, which can be attributed to a shift of the band edges to higher energy, due to the coupling of the plasmonic nanoparticle and the semiconductor surface [117]. Despite having a shifted band edge, which can improve the V_{OC}, this phenomenon can also decrease the electron injection efficiency, as previously seen in the J-V curves, thus explaining why more Au concentration is not beneficial for this application.

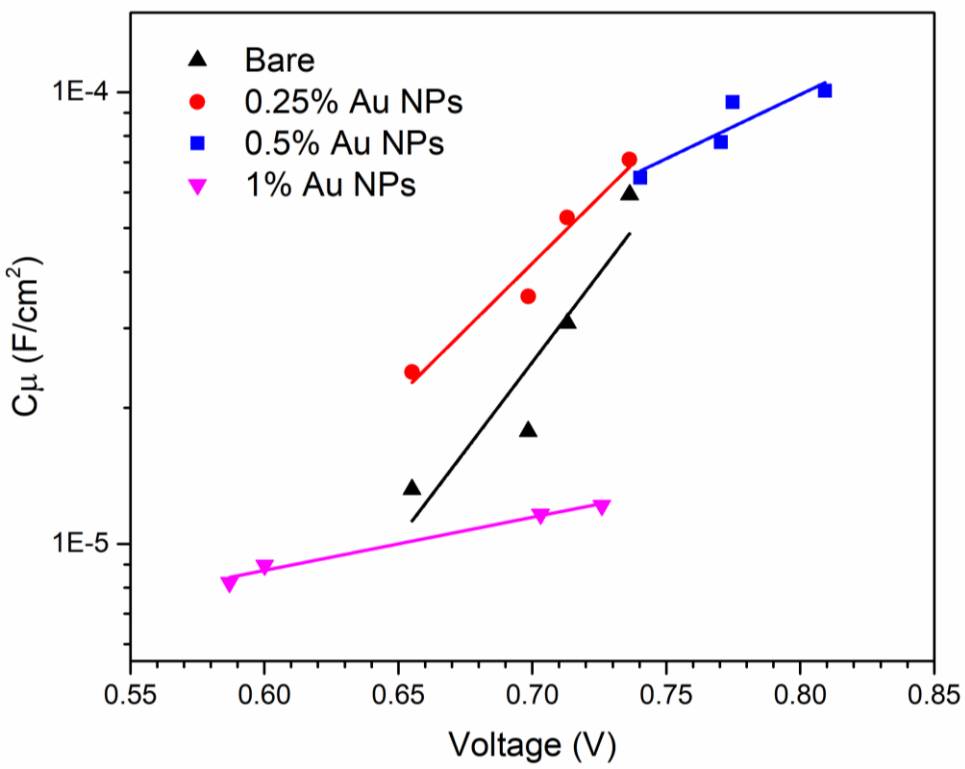

Figure 36. Chemical capacitance vs open circuit voltage of DSSC based on bare and Au decorated $ZnTiO_3$.

The recombination kinetics can be determined by plotting R_{CT} vs the open circuit voltage, as shown in Figure 37. The behavior exhibited by the graphs demonstrates that the R_{CT} decreases with the illumination intensity, indicating that the recombination is boosted which is expected. As foreseen, the solar cell with 0.5% of Au NPs has the lowest R_{CT}, and the device assembled without Au NPs has the highest resistance. It is important to note that these results should be compared at the same voltage, thus the linear fit helps to visually extrapolate the data. This result agrees with previous studies [74,119,136]. The observed behavior for the 0.5 and 0.25% Au NPs devices could be attributed to the improved charge-transfer process propitiated by the plasmonic properties of the Au NPs. Nonetheless, it can be

inferred that upon higher incorporation the recombination kinetics is enhanced due to the greater concentration of electrons transferred from the plasmonic nanoparticle to the conduction band of the semiconductor, thus an increased R_{CT} is achieved with 1% Au NPs incorporation.

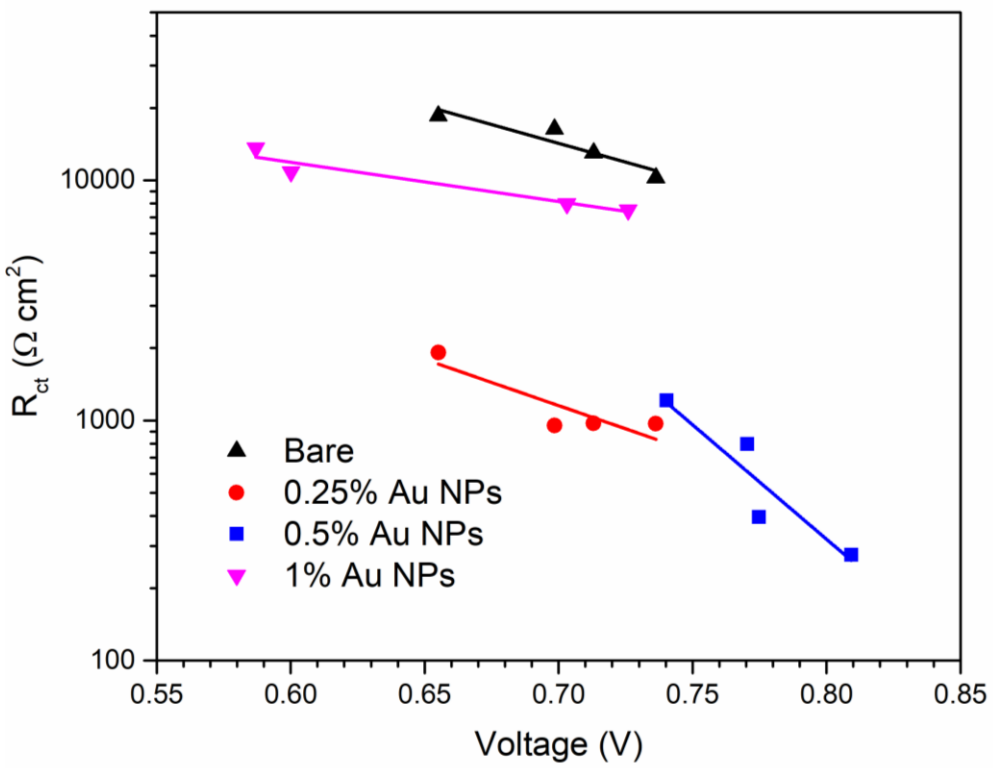

Figure 37. Recombination resistance (R_{CT}) vs voltage of DSSC based on bare and Au decorated $ZnTiO_3$.

To further evaluate the recombination kinetics the electron lifetime for each device has been determined from the Equation 18 [137] and the results are graphed in Figure 38.

$$\tau = R_{CT} C_{\mu} \qquad \text{Eq. 18}$$

The results of electron lifetime vs voltage follow the same trend as the R_{CT}, proving that the recombination kinetics are enhanced with the presence of Au nanoparticles. Especially, the sample with 1% Au NPs has a flatter slope, corroborating the results of R_{CT} and proving that a high plasmonic nanoparticle loading alters the trap distributions. The most efficient DSSC, sample 0.5% Au NPs has a lower τ than the bare sample, nonetheless it exhibits a larger V_{OC}. This behavior corroborates that the increase in performance can be attributed to an adjustment of the Fermi level upon the incorporation of the Au NPs.

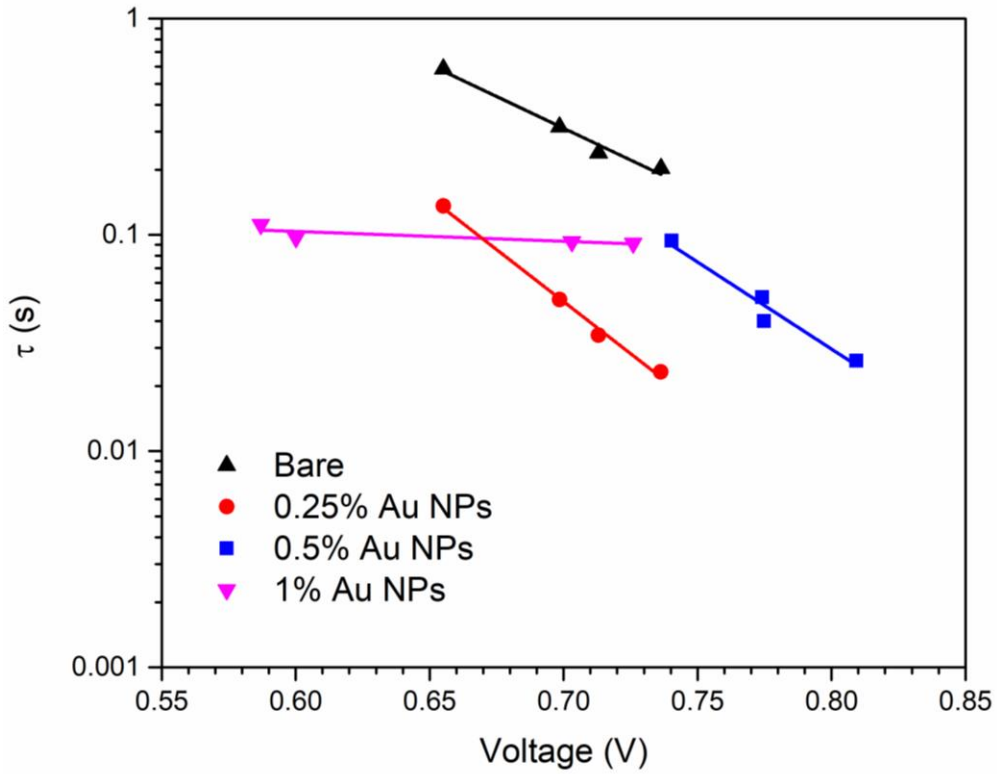

Figure 38. Electron lifetime vs voltage of DSSC based on bare and Au decorated $ZnTiO_3$.

Finally, in the Table 11 is shown a comparison with similar works that use zinc titanates or ZnO-TiO_2 as a photoanode material in DSSC or QDSSC.

Table 11. Photovoltaic parameters of solar cells with similar photoanode materials.

Type of solar cell	Photoanode material	V_{OC} (V)	J_{SC} (mA/cm^2)	FF	η%	Ref.
DSSC	$ZnTiO_3$	0.63 ± 0.16	0.31 ± 0.02	0.4 ± 0.02	0.09 ± 0.01	This work
DSSC	Au-decorated $ZnTiO_3$	0.78 ± 0.009	0.5 ± 0.08	0.47 ± 0.04	0.18 ± 0.017	This work
DSSC	TiO_2-ZnO	0.58	0.62	0.42	0.15	[138]
QDSSC	Zn_2TiO_4-$Zn_2Ti_3O_8$	0.69 ± 0.03	2.2 ± 0.3	0.4 ± 0.02	0.62 ± 0.1	[139]
QDSSC	Zn_2TiO_4-$ZnTiO_3$	0.55 ± 0.02	0.76 ± 0.10	0.33 ± 0.01	0.15 ± 0.02	[139]
DSSC	$ZnTiO_3$	0.32	4	0.62	0.079	[66]

CHAPTER 5

CONCLUSIONS

We have demonstrated that is feasible to synthesize $ZnTiO_3$ monodispersed nanoparticles by sol-gel method in air atmosphere and without surfactants or templates. The synthesized $ZnTiO_3$ nanostructures have a particle size distribution of 39.2 ± 9.8 nm, a specific surface area of 13.96 m^2/g, and band gap energy of 3.08 eV. Additionally, larger and polydisperse particles can be synthesized by the variation of the dissolution of the Zn precursor due to the availability of hydroxy ions in the reaction medium. Moreover, the yielded N719 dye loading capacity of 93 ± 4.3 $nmol/cm^2$ of $ZnTiO_3$ nanoparticles is similar to that of traditional DSSC photoanode materials.

The coupling of the synthesized $ZnTiO_3$ nanostructures with Au nanoparticles alter the optoelectronic properties of the semiconductor by deviating the quasi-Fermi level to more negative potentials, thus assisting in the electron-hole separation and shifting the trap distributions in the composite. Hence, the best optoelectronic properties have been obtained with an incorporation of 1300 ppm.

A DSSC based on Au-decorated $ZnTiO_3$ has been assembled and characterized achieving an energy conversion efficiency of 0.18%, a 200% increase compared to a DSSC based on bare $ZnTiO_3$. The photovoltaic and electrochemical characterizations proved that the performance enhancement can be attributed to the increase in the V_{OC} and the J_{SC}. The enhancement in the V_{OC} has been attributed to the shift of the quasi-Fermi level due to the presence of Au NPs, whilst the boost in J_{SC} can be ascribed to the enlarged photon absorption assisted by the near-field enhancement due to the LSPR of the Au.

REFERENCES

[1] K. A. Karpov, “Development trends of global energy consumption,” *Stud. Russ. Econ. Dev.*, (2019), https://doi.org/10.1134/S1075700719010088.

[2] G. Althor, J. E. M. Watson, and R. A. Fuller, “Global mismatch between greenhouse gas emissions and the burden of climate change,” *Sci. Rep.*, (2016), https://doi.org/10.1038/srep20281.

[3] S. Li, R. T. Bush, I. R. Santos, Q. Zhang, K. Song, R. Mao, Z. Wen, and X. X. Lu, “Large greenhouse gases emissions from China’s lakes and reservoirs,” *Water Res.*, (2018), https://doi.org/10.1016/j.watres.2018.09.053.

[4] E. Pérez-Denicia, F. Fernández-Luqueño, D. Vilariño-Ayala, L. Manuel Montaño-Zetina, and L. A. Maldonado-López, “Renewable energy sources for electricity generation in Mexico: a review,” *Renew. Sustain. Energy Rev.*, (2017), https://doi.org/10.1016/j.rser.2017.05.009.

[5] D. Sengupta, P. Das, B. Mondal, and K. Mukherjee, “Effects of doping, morphology and film-thickness of photo-anode materials for dye sensitized solar cell application - a review,” *Renew. Sustain. Energy Rev.*, (2016), https://doi.org/10.1016/j.rser.2016.01.104.

[6] M. A. Vega-Sanchez, P. D. Castaneda-Jimenez, R. Pena-Gallardo, A. Ruiz-Alonso, J. A. Morales-Saldana, and E. R. Palacios-Hernandez, “Evaluation of complementarity of wind and solar energy resources over Mexico using an image processing approach,” *IEEE International Autumn Meeting on Power, Electronics and Computing*, (2017) https://doi.org/10.1109/ROPEC.2017.8261637.

[7] A. Khatibi, F. Razi Astaraei, and M. H. Ahmadi, “Generation and combination of the solar cells: a current model review,” *Energy Sci. Eng.*, (2019), https://doi.org/10.1002/ese3.292.

[8] J. Wu, Z. Lan, J. Lin, M. Huang, Y. Huang, L. Fan, and G. Luo, “Electrolytes in dye-sensitized solar cells,” *Chem. Rev.*, (2015), https://doi.org/10.1021/cr400675m.

[9] G. Richhariya, A. Kumar, P. Tekasakul, and B. Gupta, “Natural dyes for dye sensitized solar cell: a review,” *Renew. Sustain. Energy Rev.*, (2017), https://doi.org/10.1016/j.rser.2016.11.198.

[10] D. Widhiyanuriyawan, P. Trihutomo, S. Soeparman, and L. Yuliati, “Zwitterion effect of cow brain protein towards efficiency mprovement of dye-sensitized solar cell (DSSC),” *Sci. World J.*, (2020), https://doi.org/10.1155/2020/7910702.

[11] H. Hug, M. Bader, P. Mair, and T. Glatzel, “Biophotovoltaics: natural pigments in dye-sensitized solar cells,” *Appl. Energy*, (2014), https://doi.org/10.1016/j.apenergy.2013.10.055.

[12] Z. Arifin, S. Soeparman, D. Widhiyanuriyawan, and S. Suyitno, “Performance enhancement of dye-sensitized solar cells using a natural sensitizer,” *Int. J. Photoenergy*, (2017), https://doi.org/10.1155/2017/2704864.

[13] K. Pugazhendhi, S. D'Almeida, P. N. Kumar, J. S. Selva Mary, T. Tenkyong, D. J. Sharmila, J. Madhavan, and J. M. Shyla, “Hybrid TiO_2/ZnO and TiO_2/Al plasmon impregnated ZnO nanocomposite photoanodes for DSSCs: synthesis and characterisation,” *Mater. Res. Express*, (2018), https://doi.org/10.1088/2053-1591/aab7af.

[14] S. Borbón, S. Lugo, D. Pourjafari, N. Pineda Aguilar, G. Oskam, and I. López, “Open-circuit voltage (V_{OC}) enhancement in TiO_2-based DSSCs: incorporation of ZnO nanoflowers and Au nanoparticles,” *ACS Omega*, (2020), https://doi.org/10.1021/acsomega.0c00794.

[15] N. Prabavathy, S. Shalini, R. Balasundaraprabhu, D. Velauthapillai, S. Prasanna, and N. Muthukumarasamy, “Enhancement in the photostability of natural dyes for dye-sensitized solar cell (DSSC) applications: a review,” *Int. J. Energy Res.*, (2017), https://doi.org/10.1002/er.3703.

[16] A. Carella, F. Borbone, and R. Centore, “Research progress on photosensitizers for DSSC,” *Front. Chem.*, (2018), https://doi.org/10.3389/fchem.2018.00481.

[17] S. Sharma, B. Siwach, S. K. Ghoshal, and D. Mohan, “Dye sensitized solar cells: from genesis to recent drifts,” *Renew. Sustain. Energy Rev.*, (2017), https://doi.org/10.1016/j.rser.2016.11.136.

[18] G. Calogero, A. Bartolotta, G. Di Marco, A. Di Carlo, and F. Bonaccorso, “Vegetable-based dye-sensitized solar cells,” *Chem. Soc. Rev.*, (2015), https://doi.org/10.1039/C4CS00309H.

[19] Y. Sun, A. C. Onicha, M. Myahkostupov, and F. N. Castellano, “Viable alternative to N719 for dye-sensitized solar cells,” *ACS Appl. Mater. Interfaces*, (2010), https://doi.org/10.1021/am100311m.

[20] J. Wu, Z. Lan, J. Lin, M. Huang, Y. Huang, L. Fan, G. Luo, Y. Lin, Y. Xie, and Y. Wei, “Counter electrodes in dye-sensitized solar cells,” *Chem. Soc. Rev.*, (2017), https://doi.org/10.1039/c6cs00752j.

[21] U. Ahmed, M. Alizadeh, N. A. Rahim, S. Shahabuddin, M. S. Ahmed, and A. K. Pandey, “A comprehensive review on counter electrodes for dye sensitized solar cells: a special focus on Pt-TCO free counter electrodes,” *Sol. Energy*, (2018), https://doi.org/10.1016/j.solener.2018.10.010.

[22] M. S. Ahmad, A. K. Pandey, and N. A. Rahim, “Advancements in the development of TiO_2 photoanodes and its fabrication methods for dye sensitized solar cell (DSSC) applications: a review,” *Renew. Sustain. Energy Rev.*, (2017), https://doi.org/10.1016/j.rser.2017.03.129.

[23] J. Wan, L. Tao, B. Wang, J. Zhang, H. Wang, and P. D. Lund, “A facile method

to produce TiO_2 nanorods for high-efficiency dye solar cells," *J. Power Sources*, (2019), https://doi.org/10.1016/j.jpowsour.2019.227012.

[24] B. Kiliç, N. Gedik, S. P. Mucur, A. S. Hergul, and E. Gür, "Band gap engineering and modifying surface of TiO_2 nanostructures by Fe_2O_3 for enhanced-performance of dye sensitized solar cell," *Mater. Sci. Semicond. Process.*, (2015), https://doi.org/10.1016/j.mssp.2014.12.020.

[25] S. T. Kochuveedu, J. H. Oh, Y. R. Do, and D. H. Kim, "Surface-plasmon-enhanced band emission of ZnO nanoflowers decorated with Au nanoparticles," *Chem. - A Eur. J.*, (2012), https://doi.org/10.1002/chem.201200054.

[26] E. J. Canto-Aguilar, M. Rodríguez-Pérez, R. García-Rodríguez, F. I. Lizama-Tzec, A. T. De Denko, F. E. Osterloh, and G. Oskam, "ZnO-based dye-sensitized solar cells : effects of redox couple and dye aggregation," *Electrochim. Acta* (2017), https://doi.org/10.1016/j.electacta.2017.11.075.

[27] J. Patwari, S. Shyamal, T. Khan, H. Ghadi, C. Bhattacharya, S. Chakrabarti, S. K. Pal, "Inversion of activity in DSSC for TiO_2 and ZnO photo-anodes depending on the choice of sensitizer and carrier dynamics," *J. Lumin.*, (2018), https://doi.org/10.1016/j.jlumin.2018.11.012.

[28] M. Rodríguez-Pérez, E. Canto, R. García-Rodríguez, A. T. De Denko, G. Oskam, and F. E. Osterloh, "Surface photovoltage spectroscopy resolves interfacial charge separation efficiencies in ZnO dye-sensitized solar cells," *J. Phys. Chem. C*, (2018), https://doi.org/10.1021/acs.jpcc.7b11727.

[29] R. Vittal and K. C. Ho, "Zinc oxide based dye-sensitized solar cells: a review," *Renew. Sustain. Energy Rev.*, (2017), https://doi.org/10.1016/j.rser.2016.11.273.

[30] J. Idígoras, M. Godfroy, D. Joly, A. Todinova, P. Maldivi, G. Oskam, R. Demadrille, and J.A. Anta, "Organic dyes for the sensitization of nanostructured ZnO photoanodes: effect of the anchoring functions," *RSC Adv.*, (2015), https://doi.org/10.1039/C5RA11762C.

[31] H.-M. Cheng, W.-H. Chiu, C.-H. Lee, S.-Y. Tsai, and W.-F. Hsieh, "Formation of branched ZnO nanowires from solvothermal method and dye-sensitized solar cells applications," *J. Phys. Chem. C*, (2008), https://doi.org/10.1021/jp805239k.

[32] J. Z. Ou, R. A. Rani, M.-H. Ham, M.R. Field, Y. Zhang, H. Zheng, P. Reece, S. Zhuiykov, S. Sriram, M. Bhaskaran, R. B. Kaner, and K. Kalantar-zadeh, "Elevated temperature anodized Nb_2O_5: A photoanode material with exceptionally large photoconversion efficiencies," *ACS Nano*, (2012), https://doi.org/10.1021/nn300408p.

[33] H. J. Snaith and C. Ducati, "SnO_2-Based dye-sensitized hybrid solar cells exhibiting near unity absorbed photon-to-electron conversion efficiency," *Nano Lett.*, (2010), https://doi.org/10.1021/nl903809r.

[34] H. Zheng, Y. Tachibana, and K. Kalantar-Zadeh, “Dye-sensitized solar cells based on WO_3,” *Langmuir*, (2010), https://doi.org/10.1021/la103692y.

[35] K. Sarkar, E. V. Braden, T. Fröschl, N. Hüsing, and P. Müller-Buschbaum, “Spray-deposited zinc titanate films obtained via sol-gel synthesis for application in dye-sensitized solar cells,” *J. Mater. Chem. A*, (2014), https://doi.org/10.1039/c4ta02031f.

[36] D. P. Dutta, A. Singh, and A. K. Tyagi, “Ag doped and Ag dispersed nano $ZnTiO_3$: improved photocatalytic organic pollutant degradation under solar irradiation and antibacterial activity,” *J. Environ. Chem. Eng.*, (2014), https://doi.org/10.1016/j.jece.2014.09.015.

[37] B. Ozturk and G. S. P. Soylu, “Promoting role of transition metal oxide on $ZnTiO_3$-TiO_2 nanocomposites for the photocatalytic activity under solar light irradiation,” *Ceram. Int.*, (2016), https://doi.org/10.1016/j.ceramint.2016.04.027.

[38] J. Lu, D. Li, Y. Chai, L. Li, M, Li, Y. Zhang, and J. Liang,, “Rational design and preparation of nanoheterostructures based on zinc titanate for solar-driven photocatalytic conversion of CO_2 to valuable fuels,” *Appl. Catal. B Environ.*, (2019), https://doi.org/10.1016/j.apcatb.2019.117800.

[39] H. Eskandarloo, A. Badiei, M. A. Behnajady, A. Tavakoli, and G. M. Ziarani, “Ultrasonic-assisted synthesis of Ce doped cubic-hexagonal $ZnTiO_3$ with highly efficient sonocatalytic activity,” *Ultrason. Sonochem.*, (2016), https://doi.org/10.1016/j.ultsonch.2015.10.004.

[40] J. Yu, D. Li, L. Zhu, and X. Xu, “Application of $ZnTiO_3$ in quantum-dot-sensitized solar cells and numerical simulations using first-principles theory,” *J. Alloys Compd.*, (2016), https://doi.org/10.1016/j.jallcom.2016.04.224.

[41] J. Lv, M. Tang, R. Quan, and Z. Chai, “Synthesis of solar heat-reflective $ZnTiO_3$ pigments with novel roof cooling effect,” *Ceram. Int.*, Aug. (2019), https://doi.org/10.1016/J.CERAMINT.2019.05.081.

[42] S. Ray, P. Das, B. Banerjee, A. Bhaumik, and C. Mukhopadhyay, “Cubic perovskite $ZnTiO_3$ nanopowder as a recyclable heterogeneous catalyst for the synthesis of 1,6-Naphthyridines in water,” *Chempluschem*, (2015), https://doi.org/10.1002/cplu.201402405.

[43] J. Zhuang, B. Zhang, Q. Wang, S. Guan, and B. Li, “Construction of novel - $ZnTiO_3$/g-C_3N_4 heterostructures with enhanced visible light photocatalytic activity for dye wastewater treatment,” *J. Mater. Sci. Mater. Electron.*, (2019), https://doi.org/10.1007/s10854-019-00932-x.

[44] R.S. Raveendra, P.A. Prashanth, R.H. Krishna, N.P. Bhagya, S. Sathyanarayani, and B.M. Nagabhushana, “Carbothermal synthesis and photoluminescence characteristics of pure undoped $ZnTiO_3$ nanocrystals" *Journal of Advanced Physical Sciences*,” (2016), https://www.jacsdirectory.com/journal-of-advanced-physical-

sciences/articleview.php?id=1#tab4.

[45] N. Pal, M. Paul, and A. Bhaumik, “New mesoporous perovskite $ZnTiO_3$ and its excellent catalytic activity in liquid phase organic transformations,” *Appl. Catal. A Gen.*, (2011), https://doi.org/10.1016/j.apcata.2010.11.037.

[46] Y. L. Chai, Y. S. Chang, G. J. Chen, and Y. J. Hsiao, “The effects of heat-treatment on the structure evolution and crystallinity of $ZnTiO_3$ nano-crystals prepared by Pechini process,” *Mater. Res. Bull.*, (2008), https://doi.org/10.1016/j.materresbull.2007.06.002.

[47] M. Salavati-Niasari, F. Soofivand, A. Sobhani-Nasab, M. Shakouri-Arani, A. Yeganeh Faal, and S. Bagheri, “Synthesis, characterization, and morphological control of $ZnTiO_3$ nanoparticles through sol-gel processes and its photocatalyst application,” *Adv. Powder Technol.*, (2016), https://doi.org/10.1016/j.apt.2016.07.018.

[48] S. Esposito, “‘Traditional’ sol-gel chemistry as a powerful tool for the preparation of supported metal and metal oxide catalysts,” *Materials (Basel).*, (2019), https://doi.org/10.3390/ma12040668.

[49] S. M. Sze and K. K. Ng, *Physics of semiconductor devices*. Wiley-Interscience, (2007).

[50] K. W. Böer and U. W. Pohl, *Semiconductor physics*. Springer, (2018).

[51] D. Bagayoko, “Understanding density functional theory (DFT) and completing it in practice,” *AIP Adv.*, (2014), https://doi.org/10.1063/1.4903408.

[52] H. Zhao, F. Huang, J. Hou, Z. Liu, Q. Wu, H. Cao, Q. Jing, S. Peng, and G. Cao, “Efficiency enhancement of quantum dot sensitized TiO_2/ZnO nanorod arrays solar cells by plasmonic Ag nanoparticles,” *ACS Appl. Mater. Interfaces*, (2016), https://doi.org/10.1021/acsami.6b06386.

[53] S. A. Maier, M. L. Brongersma, P. G. Kik, S. Meltzer, A. A. G. Requicha, and H. A. Atwater, “Plasmonics - A route to nanoscale optical devices,” *Adv. Mater.*, (2001), https://doi.org/10.1002/1521-4095(200110)13:19<1501::AID-ADMA1501>3.0.CO;2-Z.

[54] A. M. Glezer, “Structural Classification of nanomaterials,” *Russ. Metall.*, (2011), https://doi.org/10.1134/S0036029511040057.

[55] J. Marnocha, “Effect of Wannier-Mott exciton on semiconductor quantum dot photo-absorption spectra,” (2017).

[56] H. K. Jun, M. A. Careem, and A. K. Arof, “Plasmonic effects of quantum size gold nanoparticles on dye-sensitized solar cell,” *Mater. Today Proc.*, (2016), https://doi.org/10.1016/j.matpr.2016.01.010.

[57] H. Choi, W. T. Chen, and P. V. Kamat, “Know Thy nano neighbor . Plasmonic versus electron charging effects of metal nanoparticles in dye-sensitized,” *ACS Nano*, (2012), https://doi.org/10.1021/nn301137r.

[58] B. O'Regan and M. Gratzel, "A low-cost, high-efficiency solar-Cell based on dye-sensitized colloidal TiO_2 films," *Nature*, (1991), https://doi.org/10.1038/353737a0.

[59] M. Calvin, "Solar energy by photosynthesis," *Science*, (1974), https://doi.org/10.1126/science.184.4134.375.

[60] K. Sharma, V. Sharma, and S. S. Sharma, "Dye-sensitized solar cells: fundamentals and current status," *Nanoscale Res. Lett.*, (2018), https://doi.org/10.1186/s11671-018-2760-6.

[61] Ü. Özgür, Y. I. Alivov, C. Liu, A. Teke, M.A. Reshchikov, S. Dogan, V. Avrutin, S.-J. Cho, and H. Morkoç, "A comprehensive review of ZnO materials and devices," *J. Appl. Phys.*, (2005), https://doi.org/10.1063/1.1992666.

[62] H. R. Pant, B. Pant, R. K. Sharma, A. Amarjargal, H. J. Kim, C. H. Park, L. D. Tijing, and C. S. Kim, "Antibacterial and photocatalytic properties of Ag/TiO_2/ZnO nano-flowers prepared by facile one-pot hydrothermal process," *Ceram. Int.*, (2013), https://doi.org/10.1016/j.ceramint.2012.07.097.

[63] H. Cai, Q. You, Z. Hu, Z. Duan, Y. Cui, J. Sun, N. Xu, and J. Wu, "Fabrication and correlation between photoluminescence and photoelectrochemical properties of vertically aligned ZnO coated TiO_2 nanotube arrays," *Sol. Energy Mater. Sol. Cells*, (2014), https://doi.org/10.1016/j.solmat.2014.01.033.

[64] H. Cai, P. Liang, Z. Hu, L. Shi, X. Yang, J. Sun, N. Xu, and J. Wu, "Enhanced photoelectrochemical activity of ZnO-Coated TiO_2 nanotubes and its dependence on ZnO coating thickness," *Nanoscale Res. Lett.*, (2016), https://doi.org/10.1186/s11671-016-1309-9.

[65] Y. Wang, Y. Z. Zheng, S. Lu, X. Tao, Y. Che, and J. F. Chen, "Visible-light-responsive TiO_2-coated ZnO:I nanorod array films with enhanced photoelectrochemical and photocatalytic performance," *ACS Appl. Mater. Interfaces*, (2015), https://doi.org/10.1021/acsami.5b00980.

[66] M. H. Habibi, M. Mikhak, M. Zendehdel, and M. Habibi, "Influence of nanostructured zinc titanate, zinc oxide or titanium dioxide thin film coated on fluorine doped tin oxide as working electrodes for dye-sensitized solar cell," *Int. J. Electrochem. Sci.* , (2012), http://www.electrochemsci.org/papers/vol7/7086787.pdf.

[67] B. C. Serban, M. Bumbac, O. Ionescu, V. Dumitru, M. Brezeanu, O.Buiu, and C. Cobianu, "Quantum dots versus dyes in sensitized solar cells : synthesis , optimization , performance," in *Science and applications of Tailored Nanostructures*, P. Di Sia, Ed. One Central Press (OCP), (2017), pp. 89–127.

[68] S. Noor, S. Sajjad, S. A. K. Leghari, S. Shaheen, and A. Iqbal, "ZnO/TiO_2 nanocomposite photoanode as an effective UV-vis responsive dye sensitized solar cell," *Mater. Res. Express*, (2018), https://doi.org/10.1088/2053-1591/aad8ee.

[69] K. Cherifi, A. Cheknane, A. Benghia, H. S. Hilal, K. Rahmoun, B. Benyoucef, and S. Goumri-Said,, “Exploring N3 ruthenium dye adsorption onto $ZnTiO_3$ (101) and (110) surfaces for dye sensitized solar cell applications: full computational study,” *Mater. Today Energy*, (2019), https://doi.org/10.1016/j.mtener.2019.04.013.

[70] K. Cherifi, A. Cheknane, H. S.Hilal, A. Benghia, K. Rahmoun, and B. Benyoucef, “Investigation of triphenylamine-based sensitizer characteristics and adsorption behavior onto $ZnTiO_3$ perovskite (101) surfaces for dye-sensitized solar cells using first-principle calculation,” *Chem. Phys.*, (2020), https://doi.org/10.1016/j.chemphys.2019.110595.

[71] M. Sarkar, S. Sarkar, A. Biswas, S. De, P. R. Kumar, E. M. Mothi, and A. Kathiravan,, “Zinc titanate nanomaterials—photocatalytic studies and sensitization of hydantoin derivatized porphyrin dye,” *Nano-Structures and Nano-Objects*, (2020), https://doi.org/10.1016/j.nanoso.2019.100412.

[72] Y. W. Wang, P. H. Yuan, C. M. Fan, Y. Wang, G. Y. Ding, and Y. F. Wang, “Preparation of zinc titanate nanoparticles and their photocatalytic behaviors in the photodegradation of humic acid in water,” *Ceram. Int.*, (2012), https://doi.org/10.1016/j.ceramint.2012.01.078.

[73] Y. H. Yu and M. Xia, “Preparation and characterization of $ZnTiO_3$ powders by sol-gel process,” *Mater. Lett.*, (2012), https://doi.org/10.1016/j.matlet.2012.02.113.

[74] H. Elbohy, M. R. Kim, A. Dubey, K.M. Reza, D. Ma, J. Zai, X. Qian, and Q. Qiao, “Incorporation of plasmonic Au nanostars into photoanodes for high efficiency dye-sensitized solar cells,” *J. Mater. Chem. A*, (2016), https://doi.org/10.1039/c5ta06425b.

[75] N. Chander, A.F. Khan, E. Thouti, S. K. Sardana, P.S. Chandrasekhar, V. Dutta, V. K. Komarala, “Size and concentration effects of gold nanoparticles on optical and electrical properties of plasmonic dye sensitized solar cells,” *Sol. Energy*, (2014), https://doi.org/10.1016/j.solener.2014.08.011.

[76] W. L. Liu, F.-C. Lin, Y.-C. Yang, C.-H. Huang, S. Gwo, M.H. Huang, and J.-S. Huang, “The influence of shell thickness of $Au@TiO_2$ core-shell nanoparticles on the plasmonic enhancement effect in dye-sensitized solar cells,” *Nanoscale*, (2013), https://doi.org/10.1039/c3nr02800c.

[77] S. Koussi-Daoud, D. Schaming, P. Martin, and J. C. Lacroix, “Gold nanoparticles and poly(3,4-ethylenedioxythiophene) (PEDOT) hybrid films as counter-electrodes for enhanced efficiency in dye-sensitized solar cells,” *Electrochim. Acta*, (2014), https://doi.org/10.1016/j.electacta.2014.01.154.

[78] Q. Liu, Y. Wei, M. Z. Shahid, M. Yao, B. Xu, G. Liu, K. Jiang, C. Li,, “Spectrum-enhanced Au@ZnO plasmonic nanoparticles for boosting dye-sensitized solar cell performance,” *J. Power Sources*, (2018), https://doi.org/10.1016/j.jpowsour.2018.01.089.

[79] V. Dhas, S. Muduli, W. Lee, S.-H. Han, and S. Ogale, “Enhanced conversion efficiency in dye-sensitized solar cells based on ZnO bifunctional nanoflowers loaded with gold nanoparticles,” *Appl. Phys. Lett.*, (2008), https://doi.org/10.1063/1.3049131.

[80] J. Villanueva-Cab, P. Olalde-Velasco, A. Romero-Contreras, Z. Zhuo, F. Pan, S. E. Rodil, W. Yang, and U. Pal, “Photocharging and band gap narrowing effects on the performance of plasmonic photoelectrodes in dye-sensitized solar cells,” *ACS Appl. Mater. Interfaces*, (2018), https://doi.org/10.1021/acsami.8b10063.

[81] K. H. Reddy, S. Martha, and K. M. Parida, “Erratic charge transfer dynamics of Au/$ZnTiO_3$ nanocomposites under UV and visible light irradiation and their related photocatalytic activities,” *Nanoscale*, (2018), https://doi.org/10.1039/c8nr06158k.

[82] L. Khatua, R. Panda, R. Govindraj, and N. Santhosh, “Comparison of performance of dye- sensitized solar cell prepared with uncalcinated and calcinated ZnO-TiO_2 mixed phase nanoparticles comparison of performance of dye-sensitized solar cell prepared with uncalcinated and calcinated ZnO-TiO_2,” (2018), https://doi.org/10.1063/1.5032436.

[83] W. Zhang, S. Chang, S. Yao, and H. Wang, “Preparation and characterization of submicron star-like ZnO as light scattering centers for combination with ZnO Nanoparticles for dye-sensitized solar cells,” *J. Electron. Mater.*, (2019), https://doi.org/10.1007/s11664-019-07278-4.

[84] G. P. Musa, “Dye Sensitized Solar cells incorporated with TiO_2-ZnO Nanoparticles,” (2018).

[85] M. P. Subramaniam, G. Arunachalam, R. Kandasamy, P. Veluswamy, and · Ikeda Hiroya, “Effect of pH and annealing temperature on the properties of tin oxide nanoparticles prepared by sol-gel method,” *J. Mater. Sci. Mater. Electron.*, https://doi.org/10.1007/s10854-017-7959-2.

[86] J. Arin, S. Thongtem, A. Phuruangrat, and T. Thongtem, “Characterization of ZnO–TiO_2 and zinc titanate nanoparticles synthesized by hydrothermal process,” *Res. Chem. Intermed.*, (2017), https://doi.org/10.1007/s11164-016-2818-y.

[87] T. Bernert, J. Ruiz-Fuertes, L. Bayarjargal, and B. Winkler, “Synthesis and high (pressure, temperature) stability of $ZnTiO_3$ polymorphs studied by Raman spectroscopy,” *Solid State Sci.*, (2015), https://doi.org/10.1016/J.SOLIDSTATESCIENCES.2015.03.014.

[88] T. Surendar, S. Kumar, and V. Shanker, “Influence of La-doping on phase transformation and photocatalytic properties of $ZnTiO_3$ nanoparticles synthesized via modified sol-gel method,” *Phys. Chem. Chem. Phys.*, (2014), https://doi.org/10.1039/c3cp53855a.

[89] S. Barboux-Doeuff. and C. Sanchez, “Synthesis and characterization of

titanium oxide-based gels synthesized from acetate modifies titanium butoxide precursors," *Mat. Res. Bull.*, (1994), https://doi.org/10.1016/0025-5408(94)90099-X.

[90] X. Jaramillo-Fierro, L. F. Capa, F. Medina, and S. González, "DFT Study of Methylene Blue Adsorption on $ZnTiO_3$ and TiO_2 Surfaces (101)," *Molecules*, (2021), https://doi.org/10.3390/molecules26133780.

[91] T. Tavakoli-Azar, A. R. Mahjoub, M. S. Sadjadi, N. Farhadyar, and M. H. Sadr, "Improving the photocatalytic performance of a perovskite $ZnTiO_3$ through $ZnTiO_3$@S nanocomposites for degradation of Crystal violet and Rhodamine B pollutants under sunlight," *Inorg. Chem. Commun.*, (2020), https://doi.org/10.1016/j.inoche.2020.108091.

[92] C. Xu, C. Lei, Y. Wang, and C. Yu, "Dendritic mesoporous nanoparticles: structure, synthesis and properties," *Angew. Chemie*, (2022), https://doi.org/10.1002/ANGE.202112752.

[93] Z. A. Garmaroudi and M. R. Mohammadi, "Plasmonic Effects of Infiltrated Silver Nanoparticles Inside TiO_2 Film: Enhanced Photovoltaic Performance in DSSCs," *J. Am. Ceram. Soc.*, (2016), https://doi.org/10.1111/jace.13923.

[94] K. E. Lee, M. A. Gomez, S. Elouatik, and G. P. Demopoulos, "Further understanding of the adsorption mechanism of N719 sensitizer on anatase TiO_2 films for DSSC applications using vibrational spectroscopy and confocal raman imaging," *Langmuir*, (2010), https://doi.org/10.1021/la100137u.

[95] Y. Chen, R. Wu, L. Lin, and W. Chang, "Novel synthesis of popcorn-like TiO_2 light scatterers using a facile solution method for efficient dye-sensitized solar cells," *J. Power Sources*, (2019), https://doi.org/10.1016/j.jpowsour.2018.12.065.

[96] W. Wang, Y. Liu, J. Sun, and L. Gao, "Nitrogen and yttrium co-doped mesoporous titania photoanodes applied in DSSCs," *J. Alloys Compd.*, (2016), https://doi.org/10.1016/j.jallcom.2015.10.254.

[97] M. Y. A. Rahman, L. Roza, S. A. M. Samsuri, and A. A. Umar, "Effect of N719 Dye Dipping Temperature on the Performance of Dye-Sensitized Solar Cell," *Russ. J. Electrochem.*, (2018), https://doi.org/10.1134/S1023193518100051.

[98] J. T. Park, D. K. Roh, W. S. Chi, R. Patel, and J. H. Kim, "Fabrication of double layer photoelectrodes using hierarchical TiO_2 nanospheres for dye-sensitized solar cells," *J. Ind. Eng. Chem.*, (2012), https://doi.org/10.1016/j.jiec.2011.11.029.

[99] P. Senthil Kumar, I. Pastoriza-Santos, B. Rodríguez-González, J. García De Abajo, and L. M. Liz-Marzán, "High-yield synthesis and optical response of gold nanostars," *IOP Publ. Nanotechnol. Nanotechnol.*, (2008), https://doi.org/10.1088/0957-4484/19/01/015606.

[100] V. Amendola, R. Pilot, M. Frasconi, O. M. Maragò, and M. A. Iatì, "Surface

plasmon resonance in gold nanoparticles: A review," *J. Phys. Condens. Matter*, (2017), https://doi.org/10.1088/1361-648X/aa60f3.

[101] H. F. Zarick, O. Hurd, J. A. Webb, C. Hungerford, W. R. Erwin, and R. Bardhan, "Enhanced efficiency in dye-sensitized solar cells with shape-controlled plasmonic nanostructures," *ACS Photonics*, (2014), https://doi.org/10.1021/ph500281v.

[102] Q. Zhu, J. Lu, Y. Wang, F. Qin, Z. Shi, and C. Xu, "Burstein-Moss effect behind Au surface plasmon enhanced intrinsic emission of ZnO microdisks," *Sci. Reports*,(2016), https://doi.org/10.1038/srep36194.

[103] S. Gahlawat, J. Singh, A. K. Yadav, and P. P. Ingole, "Exploring Burstein–Moss type effects in nickel doped hematite dendrite nanostructures for enhanced photo-electrochemical water splitting," *Phys. Chem. Chem. Phys.*, (2019), https://doi.org/10.1039/C9CP04132J.

[104] S. A. Maier, "Plasmonics: Fundamentals and applications," *Plasmon. Fundam. Appl.*, (2007), https://doi.org/10.1007/0-387-37825-1.

[105] Z. Zhang, H. Chen, C. Xing, M. Guo, F. Xu, X. Wang, H.J. Gruber, B. Zhang, and J. Tang, "Sodium citrate: a universal reducing agent for reduction / decoration of graphene oxide with au nanoparticles," *Nano Res.*, (2011), https://doi.org/10.1007/s12274-011-0116-y.

[106] Q. Wang, Q. Guo, and B. Li, "Low temperature synthesis and characterization of substitutional Na-modified $K_2Ti_6O_{13}$ nanobelts with improved photocatalytic activity under UV irradiation," *RSC Adv.*, (2015), https://doi.org/10.1039/c5ra10640k.

[107] D. R. Baer and S. Thevuthasan, "Characterization of thin films and coatings," *Handb. Depos. Technol. Film. Coatings*, (2010), https://doi.org/10.1016/B978-0-8155-2031-3.00016-8.

[108] A. Erbe, S. Nayak, Y.-H. Chen, F. Niu, M. Pander, S. Tecklenburg, C. Toparli,, "How to probe structure, kinetics, and dynamics at complex interfaces in situ and operando by optical spectroscopy," *Encycl. Interfacial Chem. Surf. Sci. Electrochem.*, (2018), https://doi.org/10.1016/B978-0-12-409547-2.14061-2.

[109] J. Fick, "Crystalline nanoparticles in glasses for optical applications," *Handb. Surfaces Interfaces Mater.*, (2001), https://doi.org/10.1016/B978-012513910-6/50041-4.

[110] J. Abraham, B. Jose, A. Jose, and S. Thomas, "Characterization of green nanoparticles from plants," *Phytonanotechnology Challenges Prospect.*, (2020), https://doi.org/10.1016/B978-0-12-822348-2.00002-4.

[111] Y. Nishikitani, S. Uchida, and T. Kubo, "Nanostructured organic bulk heterojunction solar cells," *Nanostructured Mater. Sol. Energy Convers.*, (2006), https://doi.org/10.1016/B978-044452844-5/50012-3.

[112] W. J. Yin, S. H. Wei, M. M. Al-Jassim, and Y. Yan, "Origin of the diverse

behavior of oxygen vacancies in ABO_3 perovskites: a symmetry based analysis," *Phys. Rev. B - Condens. Matter Mater. Phys.*, (2012), https://doi.org/10.1103/PhysRevB.85.201201.

[113] A. Zhang, R. Gao, L. Hu, X. Zang, R. Yang, S. Wang, S. Yao, Z. Yang, Haigang Hao, Yi-Ming Yan,, "Rich bulk oxygen vacancies-engineered MnO_2 with enhanced charge transfer kinetics for supercapacitor," *Chem. Eng. J.*, (2021), https://doi.org/10.1016/j.cej.2021.129186.

[114] M. N. Mustafa and Y. Sulaiman, "Review on the effect of compact layers and light scattering layers on the enhancement of dye-sensitized solar cells," *Sol. Energy*, (2021), https://doi.org/10.1016/j.solener.2020.12.030.

[115] M. Yahya, A. Bouziani, C. Ocak, Z. Seferoğlu, and M. Sillanpää, "Organic/metal-organic photosensitizers for dye-sensitized solar cells (DSSC): Recent developments, new trends, and future perceptions," *Dye. Pigment.*, (2021), https://doi.org/10.1016/J.DYEPIG.2021.109227.

[116] D. Devadiga, M. Selvakumar, P. Shetty, and M. S. Santosh, "Recent progress in dye sensitized solar cell materials and photo-supercapacitors: A review," *J. Power Sources*, (2021), https://doi.org/10.1016/J.JPOWSOUR.2021.229698.

[117] A. A. Shah, A. A. Umar, and M. M. Salleh, "Efficient quantum capacitance enhancement in DSSC by gold nanoparticles plasmonic effect," *Electrochim. Acta*, (2016), https://doi.org/10.1016/j.electacta.2016.02.148.

[118] W. R. Erwin, H. F. Zarick, E. M. Talbert, and R. Bardhan, "Light trapping in mesoporous solar cells with plasmonic nanostructures," *Energy Environ. Sci.*, (2016), https://doi.org/10.1039/C5EE03847B.

[119] Y. H. Jang, Y. J. Jang, S. T. Kochuveedu, M. Byun, Z. Lin, and D. H. Kim, "Plasmonic dye-sensitized solar cells incorporated with Au-TiO_2 nanostructures with tailored configurations.," *Nanoscale*, (2014), https://doi.org/10.1039/c3nr05012b.

[120] Ö. Birel, S. Nadeem, and H. Duman, "Porphyrin-based dye-sensitized solar cells (DSSCs): a review," *J. Fluoresc.*, (2017), https://doi.org/10.1007/s10895-017-2041-2.

[121] Q. Zhang, C. S. Dandeneau, X. Zhou, and G. Cao, "ZnO Nanostructures for dye-sensitized solar cells," *Adv. Mater.*, (2009), https://doi10.1002/adma.200803827.

[122] A. Lemaire, A. Perona, M. Caussanel, H. Duval, and A. Dollet, "Open-circuit voltage decay: moving to a flexible method of characterisation," *IET Circuits, Devices Syst.*, (2020), https://doi.org/10.1049/iet-cds.2020.0123.

[123] N. Kutlu, "Investigation of electrical values of low-efficiency dye-sensitized solar cells (DSSCs)," *Energy*, (2020), https://doi.org/10.1016/J.ENERGY.2020.117222.

[124] S.M. Amir-Al Zumahi, N. Arobi, M. M. Rahman, M. K. Hossain, M. A. J. Rozy,

M. Bashar, A. Amri, H. Kabir, M. A. Hossain, F. Ahmed, “Understanding the optical behaviours and the power conversion efficiency of novel organic dye and nanostructured TiO_2 based integrated DSSCs,” *Sol. Energy*, (2021), https://doi.org/10.1016/J.SOLENER.2021.07.024.

[125] H. Choi, C. Nahm, J. Kim, J. Moon, S. Nam, D.-R. Jung, B. Park,, “The effect of $TiCl_4$-treated TiO_2 compact layer on the performance of dye-sensitized solar cell,” *Curr. Appl. Phys.*, (2012), https://doi.org/10.1016/j.cap.2011.10.011.

[126] A. Sedghi, and H. N. Miankushki, “Influence of $TiCl_4$ treatment on structure and performance of dye-sensitized solar cells” *Japanese J. Appl. Phys.*, (2013), https://doi.org/10.7567/JJAP.52.075002.

[127] S. G. Adhikari, A. Shamsaldeen, and G. G. Andersson, “The effect of $TiCl_4$ treatment on the performance of dye-sensitized solar cells,” *J. Chem. Phys.*, (2019), https://doi.org/10.1063/1.5125996.

[128] O. Almora, C. I. Cabrera, J. Garcia-Cerrillo, T. Kirchartz, U. Rau, and C. J. Brabec, “Quantifying the absorption onset in the quantum efficiency of emerging photovoltaic devices,” *Adv. Energy Mater.* (2021), https://doi.org/10.1002/aenm.202100022.

[129] Q. Liu, Y. Wei, M. Z. Shahid, M. Yao, B. Xu, G. Liu, K. Jiang, and C. Li,, “Spectrum-enhanced Au@ZnO plasmonic nanoparticles for boosting dye-sensitized solar cell performance,” *J. Power Sources*, (2018), https://doi.org/10.1016/J.JPOWSOUR.2018.01.089.

[130] Q. Liu, Y. Sun, M. Yao, B. Xu, G. Liu, M. B. Hussain, K. Jiang, C. Li,, “Au@Ag@Ag_2S heterogeneous plasmonic nanorods for enhanced dye-sensitized solar cell performance,” *Sol. Energy*, (2019), https://doi.org/10.1016/J.SOLENER.2019.04.079.

[131] S. N. F. Zainudin, H. Abdullah, and M. Markom, “Electrochemical studies of tin oxide based-dye-sensitized solar cells (DSSC): a review,” *J. Mater. Sci. Mater. Electron.*, (2019), https://doi.org/10.1007/s10854-019-00929-6.

[132] E. Von Hauff, “Impedance spectroscopy for emerging photovoltaics,” *J. Phys. Chem. C*, (2019), https://doi.org/10.1021/acs.jpcc.9b00892.

[133] S. Sarker, A. J. S. Ahammad, H. W. Seo, and D. M. Kim, “Electrochemical impedance spectra of dye-sensitized solar cells: Fundamentals and spreadsheet calculation,” *Int. J. Photoenergy*, (2014), https://doi.org/10.1155/2014/851705.

[134] J. Bisquert, “Theory of the Impedance of Electron Diffusion and Recombination in a Thin Layer,” *J. Phys. Chem. B* (2001), https://doi.org/10.1021/JP011941G.

[135] U. Mehmood, H. Z. Aslam, F. A. Al-Sulaiman, A. Al-Ahmed, S. Ahmed, M. I. Malik, and M. Younas, “ Electrochemical impedance spectroscopy and photovoltaic analyses of dye-sensitized solar cells based on carbon/TiO_2 composite counter electrode ,” *J. Electrochem. Soc.*, (2016),

https://doi.org/10.1149/2.0111606JES.

[136] M. Abd-Ellah, N. Moghimi, L. Zhang, J. P. Thomas, D. McGillivray, S. Srivastava, and K. T. Leung, “Plasmonic gold nanoparticles for ZnO-nanotube photoanodes in dye-sensitized solar cell application,” *Nanoscale*, (2016), https://doi.org/10.1039/c5nr08029k.

[137] J. Bisquert, F. Fabregat-Santiago, I. Mora-Seró, G. Garcia-Belmonte, and S. Giménez, “Electron lifetime in dye-sensitized solar cells: theory and interpretation of measurements,” *J. Phys. Chem. C*, (2009), https://doi.org/10.1021/jp9037649.

[138] S. A. M. Samsuri, M. Y. A. Rahman, A. A. Umar, and M. M. Salleh, “Synthesis and characterization of TiO_2–ZnO core–shell nanograss hetero-structure and its application in dye-sensitized solar cell (DSSC),” *J. Mater. Sci. Mater. Electron.*, (2015), https://doi.org/10.1007/S10854-015-3005-4/TABLES/2.

[139] A. Sahu, R. Chaurashiya, K. Hiremath, and A. Dixit, “Nanostructured zinc titanate wide band gap semiconductor as a photoelectrode material for quantum dot sensitized solar cells,” *Sol. Energy*, (2018), https://doi.org/10.1016/J.SOLENER.2018.01.092.